Super-resolution Luminescence Micro-Spectroscopy

A nano-scale view of solar cell material photophysics

Merdasa, Aboma

2017

Document Version:
Publisher's PDF, also known as Version of record

Super-resolution Luminescence Micro-Spectroscopy

A nano-scale view of solar cell material photophysics

ABOMA JOSEPH FEKADU MERDASA
DIVISION OF CHEMICAL PHYSICS | DEPARTMENT OF CHEMISTRY | LUND UNIVERSITY

Super-resolution Luminescence Micro-Spectroscopy:

A nano-scale view of solar cell material photophysics

Aboma Joseph Fekadu Merdasa

LUND
UNIVERSITY

DOCTORAL DISSERTATION
by due permission of the Faculty of Science, Lund University, Sweden.
To be defended at lecture hall B, Kemicentrum, Naturvetarv. 14, 222 41 Lund.
Friday the 27th of January 2017 at 10:15 am.

Faculty opponent
Prof. Dr. Maria Antonietta Loi

Organization
LUND UNIVERSITY

Division of Chemical Physics
Department of Chemistry
P.O. Box 124
SE-221 00 Lund, Sweden

Author(s)
Aboma Merdasa

Document name
Doctoral Dissertation

Date of issue

Sponsoring organization

Title and subtitle

Super-resolution Luminescence Micro-Spectroscopy: A nano-scale view of solar cell material photophysics

Abstract

Optical microscopy is a fundamental tool in a range of disciplines encompassed by the physical and biological sciences. At the dawn of this millennium, a break-through was made in optical microscopy where super-resolution methods emerged and declared imaging beyond the optical diffraction limit a possibility. Most of these methods are based on fluorescence detection of single molecules. These methods found particular prominence in the life sciences where small structures could be observed inside living organisms, due to the non-invasiveness of light.

Currently, there is a growing notion that these methods can be applied in physics and chemistry to study photo-induced phenomena in materials with resolution at the nanoscale. The aim of this thesis is to explore and develop these possibilities to study energy and charge transport in functional materials interesting for light harvesting and solar-energy conversion. We present a novel wide-field super-resolution microscopy method adapted from localization microscopy. In combination with fluorescence spectroscopy, it allows for an interrogation of a material's photophysical properties down to the nanometer scale. We call the method super-resolution luminescence micro-spectroscopy (SuperLuMS).

One of the examples that we present here is a study of energy migration and trapping in individual molecular J-aggregates. We show that so-called 'outliers' (rarely occurring trap states) completely determine the exciton transport and dominate the fluorescence response. We also show that hybrid organic-inorganic perovskites are ideal objects for luminescence microscopy. These "hot" solar cell and light-emitting materials possess rich structures at scales just beyond optical diffraction limit making them an ideal "playground" for employing SuperLuMS and demonstrating its abilities.

The dynamics of charge carrier recombination in these materials is controlled by trapping and, as we demonstrate here, possess a great spatial inhomogeneity. For the first time we showed that one single trap can control the fate of charge carries in micrometer sized perovskite crystals which has important consequences for optical design of solar cells and other optoelectronic devices. We were also able to observe details of light-induced degradation and crystal phase transition in individual hybrid organic-inorganic perovskite crystals.

We believe SuperLuMS is an approach which will continue to evolve and find more diverse applications in material science.

Key words Super-resolution microscopy, single molecule spectroscopy, J-aggregates, perovskites, photophysics

Classification system and/or index terms (if any)

Supplementary bibliographical information

Language
English

ISSN and key title

ISBN 978-91-7422-496-2

Recipient's notes

Number of pages

Price

Security classification

Signature  Date 20/12/16

Super-resolution Luminescence Micro-Spectroscopy:

A nano-scale view of solar cell material photophysics

Aboma Joseph Fekadu Merdasa

LUND
UNIVERSITY

Coverphoto by Aboma Merdasa

Division of Chemical Physics
Department of Chemistry
Faculty of Science

ISBN 978-91-7422-496-2 (print)
ISBN 978-91-7422-497-9 (PDF)

Printed in Sweden by Media-Tryck, Lund University
Lund 2016

Yaadannoon kitaabaa kanaa: saba koo fi maatii koo haa ta'u…

Contents

Abstract 8
Populärvetenskaplig sammanfattning 9
List of publications 10
My contribution to the publications 11
Abbreviations 12

Chapter 1 Introduction 13
Guide to the reader 15

Chapter 2 Material Properties 17
2.1 Exciton States in J-aggregates 17
2.1.1 Perylene bisimide J-aggregates 20
2.2 Charge Carriers in Hybrid Organic-Inorganic Perovskites 22
2.2.1 Direct bandgap semiconductors 22
2.2.2 The perovskite crystal structure 24
2.2.3 Methylammonium lead iodide ($MAPbI_3$) 24
2.2.4 Trap-related dynamics in $MAPbI_3$ 25

Chapter 3 Luminescence Blinking 27
3.1 Triplet States in Single Molecules 28
3.2 Charge traps in quantum dots 29
3.3 Energy migration in 'large' emitters 30

Chapter 4 Breaking the Diffraction Limit 31
4.1 Light diffraction through circular aperture 31
4.1 Point spread function (PSF) 34
4.2 Approximations using Gaussian instead of Bessel 34
4.3 Localization microscopy 36
4.3.1 Photon economy & localization precision 36
4.4 Beyond the single emitter 38

4.4.1 Rotating elliptical Gaussian for extended emitters 38
4.4.2 Localization of extended emitters 40
4.4.3 Gaussian width of extended emitters 40
4.4.4 Beyond the diffraction limit by deconvolution 41
4.4.4 Understanding the parameters: angle & rotation 43
4.5 Super-resolution Luminescence Micro-Spectroscopy 44
Chapter 5 Experimental Setup 45
5.1 The experimental setup 46
5.1.1 Excitation 46
5.1.2 Image formation 47
5.1.2 Detection & related noise 48
5.1.3 Spectral measurements 49
5.1.2 PSF characterization 50
Chapter 6 Results & Discussion 51
6.1 Paper I: Single Lévy states in J-aggregates 51
6.2 Paper II & III: PL blinking in $MAPbI_3$ 54
6.3 Paper IV: Photo-induced degradation of $MAPbI_3$ 58
6.4 Paper V: PL enhancement of $MAPbI_3$ 61
6.5 Paper VI: Localized phases in $MAPbI_3$ nano-rods 63
Conclusions 65
Acknowledgments 67
References 69

Abstract

Optical microscopy is a fundamental tool in a range of disciplines encompassed by the physical and biological sciences. At the dawn of this millennium, a break-through was made in optical microscopy where super-resolution methods emerged and declared imaging beyond the optical diffraction limit a possibility. Most of these methods are based on fluorescence detection of single molecules. These methods found particular prominence in the life sciences where small structures could be observed inside living organisms, due to the non-invasiveness of light.

Currently, there is a growing notion that these methods can be applied in physics and chemistry to study photo-induced phenomena in materials with resolution at the nano-scale. The aim of this thesis is to explore and develop these possibilities to study energy and charge transport in functional materials interesting for light harvesting and solar-energy conversion. We present a novel wide-field super-resolution microscopy method adapted from localization microscopy. In combination with fluorescence spectroscopy, it allows for an interrogation of a material's photophysical properties down to the nanometer scale. We call the method super-resolution luminescence micro-spectroscopy (SuperLuMS).

One of the examples that we present here is a study of energy migration and trapping in individual molecular J-aggregates. We show that so-called 'outliers' (rarely occurring trap states) completely determine the exciton transport and dominate the fluorescence response. We also show that hybrid organic-inorganic perovskites are ideal objects for luminescence microscopy. These "hot" solar cell and light-emitting materials possess rich structures at scales just beyond optical diffraction limit making them an ideal "playground" for employing SuperLuMS and demonstrating its abilities.

The dynamics of charge carrier recombination in these materials is controlled by trapping and, as we demonstrate here, possess a great spatial inhomogeneity. For the first time we showed that one single trap can control the fate of charge carries in micrometer sized perovskite crystals which has important consequences for optical design of solar cells and other optoelectronic devices. We were also able to observe details of light-induced degradation and crystal phase transition in individual hybrid organic-inorganic perovskite crystals.

We believe SuperLuMS is an approach which will continue to evolve and find more diverse applications in material science.

Populärvetenskaplig sammanfattning

”Seeing is believing” är ett koncept fött ur människans oändliga nyfikenhet att veta mer. Otvivelaktigt så har modern vetenskap vuxit fram ur denna naturliga strävan efter att vilja veta mer. Från ett tidigt stadium har mikroskopi varit en hörnsten i många vetenskapsdiscipliner. Redan i ett tidigt skede filosoferade mikroskopister kring vad de minsta beståndselarna av naturen är och om vi ens kan beskåda dem med hjälp av ett mikroskop. År 1873 förklarade Ernst Abbe att naturens fundamentala lagar förhindrar direkt iakttagande av objekt som är mindra än halva våglängden av det ljus som objektet utstrålar – ljusets diffraktionsgräns. Nästan 150 år efter att denna gräns etablerats lyckades vetenskapsmän bryta denna gräns med hjälp av ett par fyndiga knep. Genom att på ett välkontrollerat sätt fästa enskilda molekyler på objektet av intresse och sen få dem att skina en åt gången så kunde man successivt lokalisera deras positioner och därmed skapa en så kallad ”super-upplöst” bild av objektet. Med dessa metoder kunde inre beståndsdelar av levande organismer på en nanometerskala studeras, vilket har under de senaste åren börjat ge svar på många frågor inom biologi och medicin. För denna bragd fick dessa vetenskapsmän Nobelpriset i Kemi år 2014.

Så vad mer kan dessa metoder användas till? Det har på senare tid vuxit fram ett intresse för att studera så kallade ”funktionella material”, som ofta används i solceller och ljusdioder. Dessa material är ofta långt större än en enskild molekyl men de processer som är intressanta att förstå kan inträffa på en väldigt liten storleksskala. Det är därför av större intresse att veta hur de små beståndsdelarna, som är del av en större ensemble ger upphov till diverse processer förknippade med exempelvis verkningsgraden av solceller.

Vi introducerar en ny metod som sammanbinder högupplöst optisk mikroskopi och spektroskopi vilket ger möjlighet att studera processer i större funktionella material på en nano-skala. Med denna metod, som vi kallar *super-resolution luminescence micro-spectroscopy* (SuperLuMS) har vi börjat studera material som kan användas för solceller och lyckats förstå vilka grundläggande processer som sker när materialet belyses med solljus. Vi har kunnat identifiera hur energin rör sig i materialet, samt förstå vilka processer som eventuellt skulle kunna hämma effektiviteten av solceller eller ljusdioder. Metoden är inte bara ämnad för solcellsmaterial utan vi är förvissade om att SuperLuMS kan hitta tillämpningar för funktionella material i allmänhet.

List of publications

I. Single Lévy States – Disorder induced energy funnels in molecular aggregates.

***Aboma Merdasa**, Angel J. Jímenez, Rafael Camacho, Matthias Meyer, Frank Würthner, and Ivan G. Scheblykin*. Nano Letters, 14 (2014), 6774-6781.

II. Giant photoluminescence blinking of perovskite nanocrystals reveals single-trap control of luminescence.

*Yuxi Tian, **Aboma Merdasa**, Maximilian Peter, Mohamed Abdellah, Kaibo Zheng, Carlito S. Ponseca Jr., Tõnu Pullerits, Arkady Yartsev, Villy Sundström, and Ivan G. Scheblykin*. Nano Letters, 15 (2015), 1603-1608.

III. 'Super-trap' at work: Extremely efficient non-radiative recombination channels in $MAPbI_3$ revealed by luminescence super-resolution imaging and spectroscopy.

***Aboma Merdasa**, Yuxi Tian, Rafael Camacho, Alexander Dobrovolsky, Elke Debroye, Eva Unger, Johan Hofkens, Villy Sundström, and Ivan G. Scheblykin*. Under review in ACS Nano.

IV. Super-resolution luminescence micro-spectroscopy reveals mechanism of photo-induced degradation in $CH_3NH_3PbI_3$ perovskite nano-crystals.

***Aboma Merdasa**, Monojit Bag, Yuxi Tian, Elin Källman, Alexander Dobrovolsky, and Ivan G. Scheblykin.* The Journal of Physical Chemistry C, 120 (2016), 10711-10719.

V. Enhanced organo-metal halide perovskite photoluminescence from nanosized defect-free crystallites and emitting site.

*Yuxi Tian, **Aboma Merdasa**, Eva Unger, Mohamed Abdellah, Kaibo Zheng, Sarah McKibbin, Anders Mikkelsen, Tõnu Pullerits, Arkady Yartsev, Villy Sundström, and Ivan G. Scheblykin*. The Journal of Physical Chemistry Letters, 6 (2015), 4171-4177.

VI. Defect-induced local variation of crystal phase transition temperature in metal halide perovskites.

*Alexander Dobrovolsky, **Aboma Merdasa**, Eva Unger, Arkady Yartsev, and Ivan G. Scheblykin.* Under review in Nature Communications.

My contribution to the publications

I. I designed the study together with IGS, prepared the samples from the dyes originally synthesized by AJ and FW, conducted all experiments, developed the super-resolution analysis procedure and analyzed all data (except 2DPOLIM conducted by RC and MM), developed the model and wrote the manuscript with IGS (with help from FW).

II. I assisted YT in the experiments, did the analysis related to super-resolution, developed the model with YT and IGS, and wrote the super-resolution part of the manuscript.

III. I designed the study together with IGS, conducted the experiments with YT and AD, analyzed all data except that related to SOFI (conducted by RC), developed the model and wrote the manuscript together with IGS.

IV. I designed the study, conducted the experiments together with YT, EK and AD, analyzed all data, developed the model and wrote the manuscript together with MB and IGS.

V. I conducted the experiments together with YT and SM, developed the analysis method for super-resolution localization of emitting sites in large crystals, developed the model with YT and IGS, and wrote the super-resolution part of the manuscript.

VI. I conducted the data analysis using super-resolution to localize emission from domains of different phase, prepared the related figures and text and helped finalize the manuscript.

Abbreviations

AFM – Atomic force microscope

APD – Avalanche photo diode

CB – Conduction band

CCD – Charge-coupled device

CT – Charge transfer (state)

CW – Continuous wave

EM-CCD – Electron multiplying CCD

FWHM – Full width at half maximum

ISC – Inter system crossing

$MAPbI_3$ – Methylammonium lead iodide

MCH – Methylcyclohexane

NA – Numerical aperture

PALM – Photo-activated localization microscopy

PBI – Perylene bisimide

PCE – Power conversion efficiency

PL – Photoluminescence

PSF – Point spread function

QD – Quantum dot

SEM – Scanning electron microscope

SM – Single molecule

SMS – Single molecule spectroscopy

ST – Surface trap (state)

STORM – Stochastic optical reconstruction microscopy

SuperLuMS – Super-resolution luminescence micro-spectroscopy

VB – Valence band

Chapter 1
Introduction

The driving force behind the evolution of microscopy has been the desire to observe objects at a smaller and smaller scale. It can be argued that it is an innate curiosity within all of us to know more about the unseen. Most of those reading this did at some point in their early life conduct a microscopic experiment through a magnifying glass with utter excitement of how much detail can be seen. Although it may seem naïve to call it an experiment, a magnifying glass at least fits well under the definition of what a microscope is. It is therefore hard to attribute the invention of microscopy to a person or even a time in history. However, the invention of the compound microscope in the all too familiar contraption we know today (the one most readers picture in their mind right now), is widely attributed to Dutch spectacle makers in the late 16th century since it was then microscopy began to evolve as a scientific discipline.

Over the last century, technological advancements have enabled an unprecedented boom in the development of microscopy methods that are today pillars in a wide range of physical and biological sciences. We are currently in the scientific era where entire disciplines rest on the ability to acquire information beyond what the naked eye can see. One of those is the field of single-molecule spectroscopy (SMS), which is fundamentally driven by the desired to inquire about what the building block of an ensemble looks like.

Although optical detection of single molecules was first demonstrated via absorption measurements,[1] it was detection by luminescence that laid the foundation for SMS to develop.[2] As such, non-invasive methods could be used to not only understand the function of a particular molecule, but also to manipulate it by light.[3] It was quickly established that a single molecule does not necessarily reflect the same optical properties as its ensemble averaged response, which is largely attributed to effects of the environment.[4–6] The ability of a single molecule to report on its environment took a new twist when fluorescent dyes could be attached onto a stationary or mobile structure in for example a living cell.[7] Rather than reporting on the environment through their photo-induced response, single molecules could provide an idea of a sample's structure in spatial regimes where conventional microscopy suffered

limitations due to the diffraction limit of light. The way was paved for optical super-resolution microscopy to emerge.

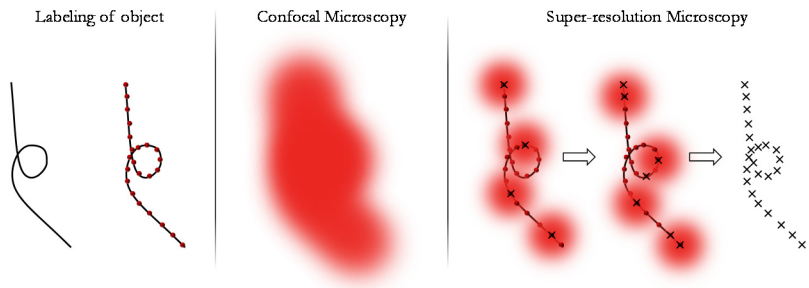

Figure 1.1. A small object (a few tens of nm) is initially labelled with fluorescent dyes (fluorophores). With confocal microscopy the exciting volume is too big and simultaneously excites all fluorophores. Super-resolution microscopy can in one way or another excite only a single fluorophore at once, determine its location and repeat the process until the location of all fluorophores are determined which then yields the object structure.

Nearly a decade ago, three independent groups demonstrated that the optical diffraction limit was broken in practice - a feat that was awarded the Nobel Prize in Chemistry 2014 (Eric Betzig,[8] William E. Moerner,[1] and Stefan Hell[9,10]) for 'the development of super-resolved fluorescence microscopy'.[11] In confocal microscopy a small volume can be excited, yet it is limited by the diffraction of light and can therefore at best excite an area of ~ 200 nm in diameter, which is much larger than a single molecule (~ 1 nm). The methodological foundation of the super-resolution methods is to determine the spatial coordinates of just one single molecule beyond the diffraction limit by its luminescence. Information beyond the diffraction limit is achieved through a combination of controlled labeling of fluorescent dyes together with some form of manipulation of the luminescence generating excitation (explained in Figure 1.1). There are currently far too many established super-resolution methods to discuss here,[12–14] but in broader strokes they can be distinguished by those that i) put emphasis on the manipulation of the excitation (deterministic methods) and ii) those that rely more on controlled labeling and post-processing of data (stochastic methods). Since their inception, these techniques have found widespread application in the life sciences.[14]

Optical super-resolution microscopy is finding its way into material science where functional materials for light harvesting is receiving attention.[15,16] In such materials, it is not necessarily of interest to understand the sub-diffraction limited spatial dimensions of an object, but more so why it may luminesce since this can report on the photophysics of the material under optical excitation. The emitting species in such materials can vary greatly in size and shape (nano- and micro-crystals, thin films), which poses difficulties for the established super-resolution methods to be

employed. Although electron and atomic force microscopy can yield sub-nanometer resolutions and characterize the structure well, these methods fail to provide insight into the operations of a material when it is exposed to Sunlight.

In this work, a new optical super-resolution method is presented which is tailored to study objects of significantly larger size than a single molecule. The novelty lies just as much in the method as well as the scientific discoveries of two classes of materials often studied in the optoelectronic scientific community. With the method, named *Super-resolution Luminescence Micro-Spectroscopy (SuperLuMS)*, we demonstrate how the photophysics of efficient light absorbers can be studied without necessarily breaking them apart into their individual building blocks, which allows them to remain in their 'natural habitat'.

Guide to the reader

Chapter 2 introduces the two materials studied in this work and provides a brief background to their most important optical properties. Chapter 3 discusses the phenomenon of blinking, as it is an important observation connected to the dynamics of the underlying photophysical properties. Blinking is also the main feature studied with SuperLuMS. Chapter 4 describes how the established methods are adapted for larger emitters while Chapter 5 briefly presents the experimental setup in which it is measured. Chapter 6 gives a summary of the results related to the two material classes introduced in Chapter 2.

Chapter 2
Material Properties

The two classes of materials addressed in this study are molecular aggregates and organic-inorganic hybrid semiconductors. Although the primary excited states in each of these materials differ, they have some common features as will be illustrated below.

2.1 Exciton States in J-aggregates

In 1936 it was observed that the absorption and luminescence spectra of cyanine dyes drastically changed when placed in an aqueous solution with high concentration of salts. It was explained that the cyanine dyes self-assemble into ordered aggregates composed of hundreds or even thousands of molecules.[17,18] Such assembly occurs via van der Waals interactions between dye molecules (monomers). J-aggregate assembly occurs via so-called *head-to-tail* stacking formation. However, the dyes can also arrange in a face-to-face formation if the solvent polarity accommodates for it (H-aggregate). The stacking formation ultimately determines the absorption spectrum shifts in relation to that of the monomer (Figure 2.1).[19]

The important feature of J-aggregates is that the excited states are formed through coupled transition dipole moments. This means that there is splitting only of the excited states and not the ground state, which is contrary to semiconductors as will be discussed below (Section 2.2). The coupling is usually approximated by dipole-dipole interaction and depends on the distance between the molecules and their relative orientation.

Considering a one-dimensional aggregate of N coupled two-level monomers possessing energetic disorder, the Frenkel exciton Hamiltonian describing that system can be written as,[20]

$$\boldsymbol{H}_{ex} = \sum_{n} (\langle E_{mon} \rangle + D_n) |n\rangle \langle n| + \sum_{n,n+1} J_{n,n+1} |n+1\rangle\langle n| \tag{2.1}$$

where $\langle E_{mon} \rangle$ is the average transition energy of the monomers and D_n is the shift of the n^{th} monomer energy from the average, which is drawn from a distribution with standard deviation, σ_D. $|n\rangle$ represents the state in which the n^{th} monomer is excited and all other monomers are in the ground state and $J_{n,n+1}$ (or just J) is the interaction between two neighboring monomers (resonance interaction) Here, the so-called nearest-neighbor model is used where interaction is only considered between adjacent monomers.[21]

In order to find the stationary states wavefunction ($\boldsymbol{\varphi}_{ex}$) of the system we need to diagonalize the Hamiltonian. The eigenvector ($\boldsymbol{\varphi}_{ex}$) has N components which determine the amplitude of the excited state wavefunction (exciton) on each monomer of the chain. In the simple head-to-tail arrangement, the squared sum of these amplitudes yields the oscillator strength (f_e) relative to the oscillator strength of the monomer (f_m). For an ideal chain without disorder (σ_D = 0, D_n= 0), the eigenstates (exciton wavefunctions) can be written as

$$|\varphi_j\rangle = \left(\frac{2}{N+1}\right)^{1/2} \sum_{n=1}^{N} \sin\left(\frac{\pi j n}{N+1}\right) |n\rangle \tag{2.2}$$

and the energies of the exciton states can be expressed analytically as,

$$E_{ex} = E_{mon} + 2J\cos\left(\frac{\pi j}{N+1}\right) \tag{2.3}$$

where j = 1, …, N. Thus, in the absence of disorder, the exciton states are delocalized over the entire aggregate. Due to the Fourier relation between position and momentum, the k-vector of the delocalized exciton wavefunction where j = 1 is well defined and ~ 0. For J-aggregates, J<0 and the state where j = 1 has the lowest energy, $E_{min} \approx E_{mon}$ - 2J (Figure 2.1). This state also has the maximum possible oscillator strength for this J-aggregate which is close to Nf_m.

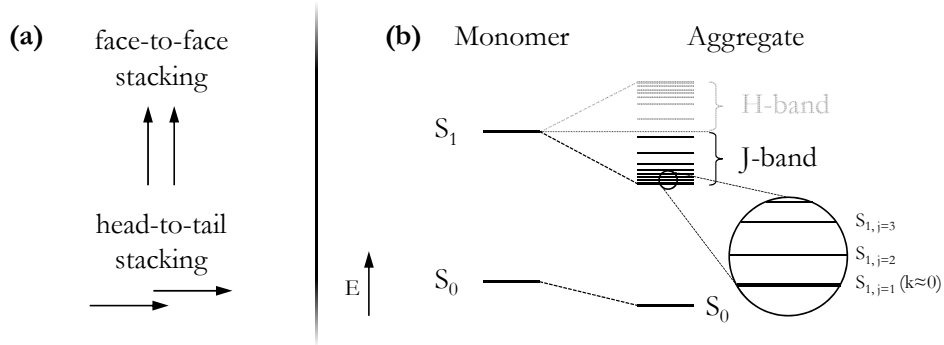

Figure 2.1 (a) Monomer transition dipole alignment for H-aggregate (face-to-face) and J-aggregate (head-to-tail) formation. (b) Exciton band structure for a J-aggregate where the lowest state is formed by coherent coupling of all monomers within the J-aggregate.

In reality, disorder is present for both the monomer energies (diagonal disorder) and for the resonance interaction (off-diagonal disorder), and the spread of the exciton wavefunction becomes limited.[20] In other words, minimizing disorder promotes coupling between more transition dipole moments. The ratio σ_D/J is used to show the degree of disorder and it is connected with exciton state delocalization length in a J-aggregate.

To study the relation between the molecular disorder and the exciton states, we generate and diagonalize the Frenkel exciton Hamiltonian using MatLab where N, E_{mon}, σ_D and J can easily be varied to observe how the exciton wavefunctions ($\boldsymbol{\varphi}_{ex}$) are distributed over the aggregate as well as their respective energies (E_{ex}) and oscillator strengths. Here we present two examples of J-aggregates with N = 250 monomers where $\sigma_D/J = 0$ (Figures 2.2a-b) and $\sigma_D/J = 0.5$ (Figures 2.2c-d).

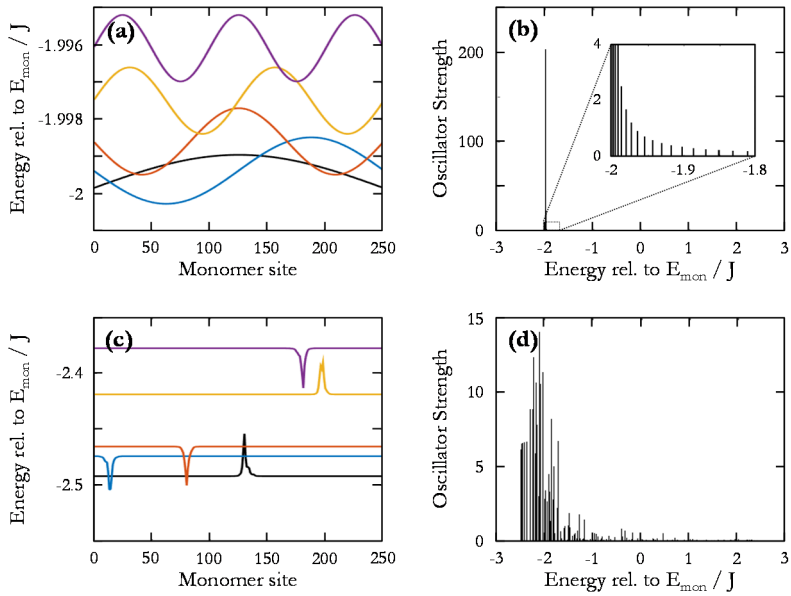

Figure 2.2 (a) Five lowest exciton states and their delocalization across the monomer sites. Here, $\sigma_D/J = 0$ and the lowest state (black) carries nearly all the oscillator strength (b). In the case where $\sigma_D/J = 0.5$, the exciton states become more localized and the oscillator strength is distributed over more states (c-d).

For $\sigma_D/J = 0$, all states delocalize across the entire J-aggregate (the five lowest states are plotted in the figure), however, only the lowest state (black) has a significant oscillator strength (Figure 2.2a). In fact, this state carries nearly the entire oscillator strength of the whole aggregate (Figure 2.2b). When disorder is introduced, exciton states become localized on fewer monomers, each having a lower, yet appreciable oscillator strength (Figure 2.2c-d).

In Paper **I**, the effects of different distributions of molecular disorder on the optical properties of J-aggregates are modeled and the results are used to interpret the fluorescence spectra of individual J-aggregates of perylene bisimide dyes.

2.1.1 Perylene bisimide J-aggregates

In this work we study J-aggregates formed by perylene bisimide (PBI) dyes originally synthesized by Kaiser et. al.[22] Unlike the classical J-aggregates of cyanine dyes that bond through van der Waals forces in aqueous solutions, PBI dyes form J-aggregates via hydrogen bonding and pi-pi stacking which can take place in organic solvents. When submersed in methylcyclohexane (MCH), PBI dyes form true linear one-dimensional J-aggregates. The large side groups (R in the figure) prevent formation of brick-wall[23] and tubular type[24] of structures common for classical J-aggregates.

To know the stacking arrangement and dimensions is of particular relevance because it connects the number of molecules in the aggregates to their linear dimension. It has been reported that excitons can migrate over ~ 100 nm along the 1D chain of PBI J-aggregates.[25] Since each dye is ~ 1.5 nm long, this distance can therefore be directly related to the number of monomers involved in the migration. PBI J-aggregates are approximately 10 nm wide and can be up to several microns in length (Figure 2.3).[22,26]

Figure 2.3c demonstrates the bathochromic shift of the absorption upon aggregation of PBI dyes. The width of the J-aggregate absorption peak (blue) is shifted by 1950 cm^{-1} from the monomer absorption (black) and has become narrower by 350 cm^{-1}.

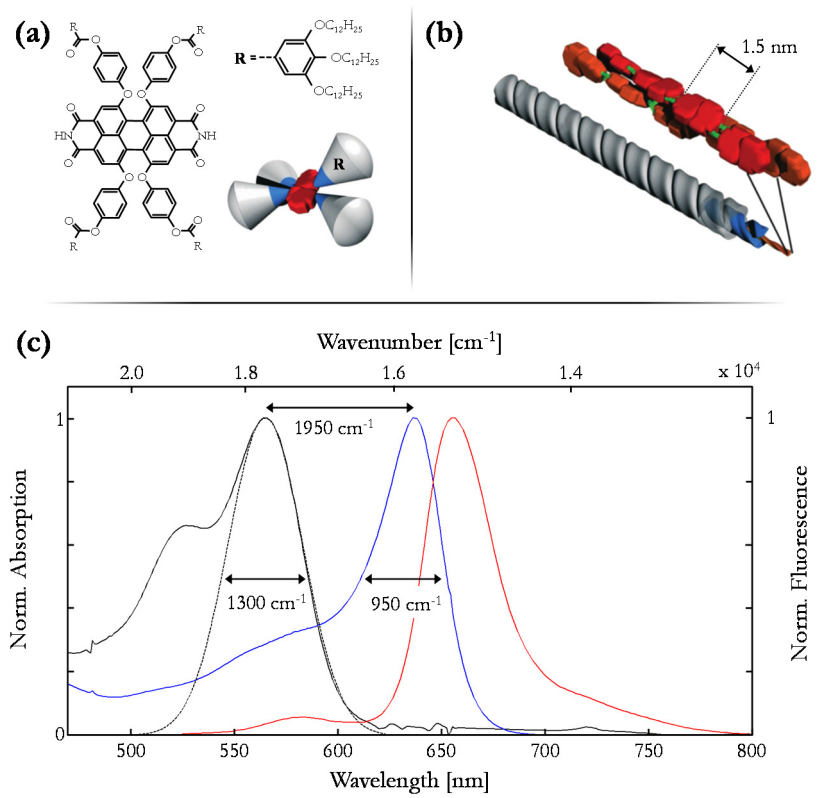

Figure 2.3 (a) PBI dye chemical structure. (b) Schematic showing the assembly into highly linear J-aggregates of thickness ~ 10 nm. Each PBI dye is about 1.5 nm long. (c) Absorption of monomer (black) as well as absorption and fluorescence of J-aggregate (blue and red respectively).

2.2 Charge Carriers in Hybrid Organic-Inorganic Perovskites

From a technological standpoint, organic solar cells are cheap to produce as materials are abundant, but the power conversion efficiencies (PCEs) are not matched with those of inorganic solar cells.[27] Hybrid organic-inorganic perovskites were initially used as sensitizers in dye-sensitized solar cells[28] but it was quickly realized that perovskite could alone serve as an efficient light harvester due to its semiconductor properties. Some of the key optical properties include broad absorption, fast charge separation (low exciton binding energy) and very slow recombination making them ideal for solar cell devices. [29–34] In addition to this, their solution-processability make them attractive for low-cost mass-production. Despite these exceptional features, there are critical hurdles relating to stability,[35] scalability[36] and toxicity[37] that must be overcome before progressing to the technological stage.

At the time of this writing, perovskite solar cells with PCEs in excess of 20% have been achieved and certified.[34,38] Notwithstanding these impressive numbers, a comprehensive understanding of the underlying photophysics in these devices have not fully been achieved. This is not due to a lack of effort but rather that the material properties, and thereby the optical properties, are very sensitive to a range of variables connected with synthesis,[39,40] ambient conditions during light exposure,[41–44] and general measurement conditions[45] to mention a few. For many of these reports, the common denominator can in one way or another be related to material defects.[46,47] The impact of defects on the photophysics in perovskites and how they relate to the microstructure of thin films[48–50] and crystals[51–53] has been of central focus in this work (Papers **II-VI**).

2.2.1 Direct bandgap semiconductors

Rather than weak van der Waals bonding between molecules, semiconductors are formed by strong covalent bonds between atoms (repeat units) in a lattice. Each repeat unit (N) has a ground and excited state (S_0 and S_1 in the two-level system approximation). Similar to the formation of the exciton band in J-aggregates, it is the interaction between the atoms in the crystal which leads to splitting of their excited and ground states into bands. As the number of atoms in the crystal increases, the density of states grows and the energy gap between the highest (S_0) and lowest (S_1) states diminishes. Figure 2.4a shows how the ground and exited states are altered as the number of repeat units increases from N = 1 to N = ∞ (bulk regime). The ground and exited states have transformed into the valence (VB) and conduction (CB) bands respectively, in which a manifold of quasi-continuous states exist.

It only really makes sense to speak of a semiconductor when N > 10 because that is when bulk properties start to be seen. However, to really be in the bulk property regime, one should expect to have at least N > 10^{10} which is the case for a semiconductor crystal with a volume of ~1 μm^3.[54]

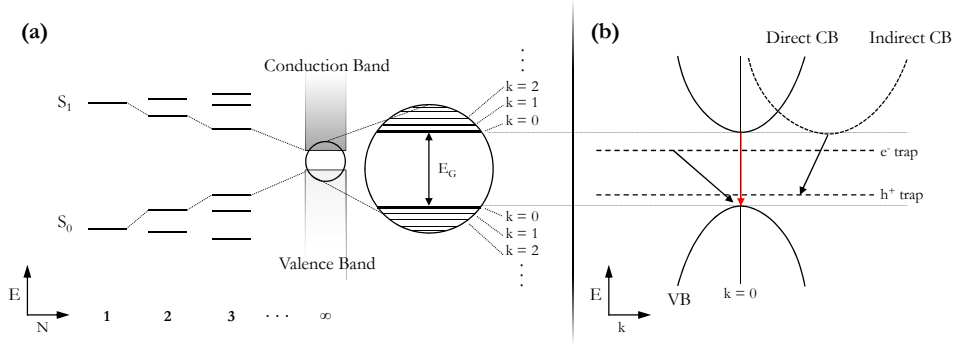

Figure 2.4. (a) Formation of the valence and conduction bands as N increases from 1 to ∞. (b) Configuration coordinate diagram showing a direct and indirect conduction band from which a recombination with a hole occurs radiatively (red arrow) and non-radiatively (black arrow) respectively. Sub-bandgap trap states are assumed to mediate non-radiative recombination as there is a mismatch between k-vectors between the electrons and holes. These states are drawn as horizontal lines in the configuration coordinate diagram since momentum is undefined.

In a semiconductor, electrons that are not participating in a lattice bond can migrate in the conduction band. The corresponding vacancy in the valence band (hole) can migrate too. Migrating charge carriers can be considered wave-packets each having a k-vector describing the direction and magnitude of the energy propagation. As a charge carrier migrates through the quasi-continuous states in either of the bands, its k-vector must change since the particle either gains or loses energy. Since the charge carrier maintains its mass, a change in energy must alter its momentum. As electrons and holes migrate through the states in either of the bands, energy is transferred between the charge carriers and phonons in the lattice environment.

When for example an electron reaches the conduction band edge it can recombine with a hole in the valence band edge and emit a photon (radiative recombination). For that to occur, the difference between the k-vectors of each charge ($\Delta\vec{k} = \vec{k}_{electron} - \vec{k}_{electron}$) must match the k-vector of a photon having energy equal to the bandgap since momentum must be conserved ($\Delta\vec{k} = \vec{k}_{photon}$). Since the momentum of a charge, $k_{e/h} = 2\pi/a$ (where a is the lattice constant), is much smaller than the momentum of a photon, $k_p = 2\pi/\lambda$ ($\lambda >> a$), a radiative recombination will only occur for $\Delta\vec{k} \approx 0$. This occurs when the conduction band and valence band minima overlap in k-space, and the material is said to have a direct bandgap. This is demonstrated in Figure 2.4b in a configuration coordinate diagram. Note that this is a simplified picture that doesn't take into account electron-phonon interactions.

2.2.2 The perovskite crystal structure

Lending its name from a Russian nobleman, Lev Perovski, the term *perovskite* was first used in 1839 to name the then newly discovered mineral, calcium titanium oxide ($CaTiO_3$). Nearly 100 years later, Victor Goldschmidt categorized a class of material having the same chemical formula as the $CaTiO_3$ compound (ABX_3) and adopted a perovskite crystal structure. The perovskite structure consists of two cations of different size and one anion. The B-cation has a 6-fold coordination with the X-anions forming an octahedron which is surrounded by a scaffold of A-cations. Figure 2.5 shows the perovskite structure arrangement of a unit cell in cubic symmetry as well as a 3-D structure of a perovskite semiconductor lattice.

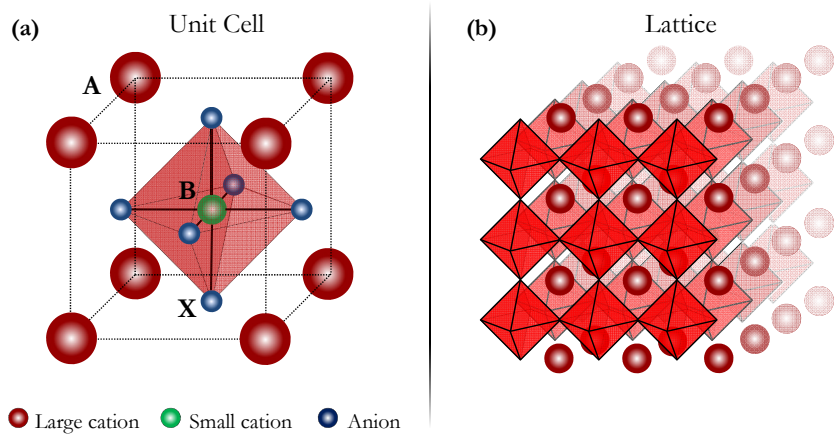

Figure 2.5. (a) Cubic symmetry of the perovskite structure where 1 B-cation and 6 X-anion form an octahedra sitting in a scaffold of 8 A-cations. (b) 3-D perovskite lattice.

2.2.3 Methylammonium lead iodide ($MAPbI_3$)

Until now, the most extensive work in the scientific community has been done on the methylammonium lead iodide ($CH_3NH_3PbI_3$ or $MAPbI_3$) perovskite compound. Halide perovskites consist of a large monovalent cation (A), such as the methylammonium ion ($CH_3NH_3^+$or MA^+), divalent cation (B), such as the lead ion (Pb^{2+}) and the anion (X), such as the iodide ion (I^-). Figure 2.5 depicts the perovskite crystal structure as a perfect cubic structure. $MAPbI_3$ adopts this crystal structure at temperatures exceeding 329 K, while at room temperature, PbI_6-octahedra become slightly distorted with respect to each other and a tetragonal crystal structure is adopted. At room temperature the $MAPbI_3$ tetragonal phase has a bandgap of E_G = 1.63 eV.[55]

Tilting the octahedra within the lattice strongly affects the bandgap energy (E_G),[56] which has been attributed to altering the angle formed by the Pb-I-Pb bonds since this is where the transition occurs. Photoluminescence spectral signatures can therefore reveal much about the material structural properties as well as the photophysical response, which has been demonstrated in both temperature dependent[57,58] and light intensity dependent measurements.[59,60] We present such studies in Papers **VI** and **IV** respectively.

One important feature of $MAPbI_3$ that in fact allows us to study many of its properties by means of its photoluminescence (PL) is that it has a direct bandgap as previously discussed. Thus the preferred recombination is radiative. Figure 2.6 shows the absorption and photoluminescence spectra of $MAPbI_3$.

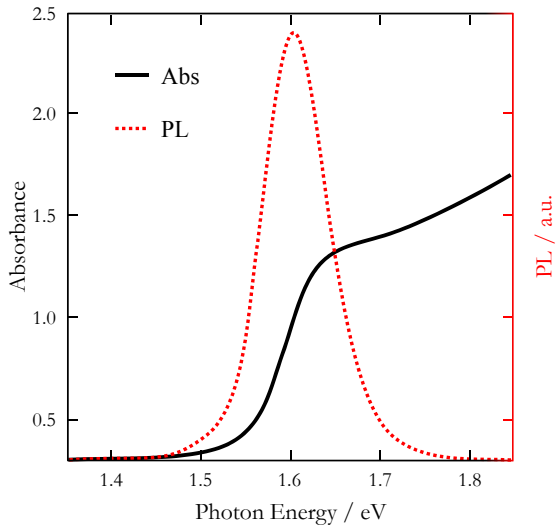

Figure 2.6. Absorption and photoluminesnce spectra of $MAPbI_3$ thin film. Data from ref 55.

2.2.4 Trap-related dynamics in $MAPbI_3$

$MAPbI_3$ has a direct bandgap and the defects form sub-bandgap states as demonstrated in Figure 2.5b. This means there is an offset of the k-vectors between a trapped electron/hole and its respective counterpart in the band, meaning that at first approximation, trap-mediated recombination occurs without emission of a photon. However, this notion is currently under debate in a very recent report where it is proposed that the $MAPbI_3$ bandgap actually has a direct-indirect character, which calls for a more complex picture beyond the scope of this thesis.[61]

The exact chemical nature of a material defect can vary greatly ranging from ionic vacancies and interstitials for each ionic specie, to structural defects and impurities. More than likely, all types of defects are present to some extent in most samples, whether it is a thin film or a crystal. Impurities can be reduced by controlling the atmosphere during synthesis and structural defects can either be reduced by precursor modification[62] or simply growing high quality crystals.[52,57,63,64] However, defect-free material is unheard of and in general, we can expect to have a defect concentration somewhere between 10^{14}-10^{18} cm^{-3}.[65–67]

In Chapter 6 we present a more detailed discussion regarding defects and their impact on the photophysics of $MAPbI_3$. Papers **II** and **III** particularly focuses on at least two different types of defects and their relative concentrations where luminescence blinking is the key reporter of the underlying photophysics in $MAPbI_3$ nano- and micro-crystals. Paper **V** sheds light on the interaction between light and oxygen impurities and how these affect the material defects. Paper **VI** discusses the effect defects may have on the temperature dependent transition between the tetragonal and orthorhombic phases.

Chapter 3
Luminescence Blinking

Blinking is the phenomenon when an emitter intermittently switches between a luminescent 'bright' state and a 'dark' state while being subject to non-intermittent excitation. Why blinking occurs can be for a range of reasons depending on the material that is blinking, its size and the environment is in. The mechanism behind blinking in single molecules, quantum dots, larger multichromophoric systems and bulk semiconductor crystals can be different to some degree. But one common thing they all share is that blinking can provide a good report on the photophysics of the material.

Blinking was in 1995 first observed in single terrylene molecules, closely followed by blinking in cadmium selenide (CdSe) quantum dots. These two systems differ both in size and in their chemical composition, thus two different blinking mechanisms were presented.[68–70] Shortly after, two independent groups demonstrated blinking in multichromophoric systems.[71,72] The underlying mechanism causing blinking in these systems again went by a different explanation since these systems were significantly larger than the previous two. The key observation that pointed to the different mechanisms was the time duration of the dark states, which ranged from milliseconds to several seconds and beyond.

Despite the different mechanisms, blinking in all aforementioned systems relate by the fact that the actual switching between states (dark/bright) occurs on much faster time scales compared to the time the system can remain in each state. In systems where long 'on/off' durations are observed (ms-s), the photophysical processes causing the switching can indirectly be studied via imaging using a charge-coupled device (CCD) camera where the temporal resolution is limited to the ms time-scale. Imaging of blinking emitters is a corner-stone in stochastic super-resolution imaging techniques.[73–76] In this thesis, blinking has been the foundation for the developed methods (Chapter 4), which also tie in spectroscopy to further reveal the photophysics of materials under constant illumination (Papers **I-IV**).

3.1 Triplet States in Single Molecules

In the simplified picture, an electron in a small single molecule (SM) goes from the singlet ground state (S_0) to the first excited state (S_1) via the absorption of a photon. The electron does not change spin, thus the excited state is also of singlet spin multiplicity and a transition back to the ground state is allowed and typically occurs within a few nanoseconds via the emission of a photon (Figure 3.1a). Non-radiative relaxation processes between S_1 and S_0 are omitted in this picture since they do not directly cause blinking. Once the electron is back in S_0, the molecule is ready to absorb another photon and repeat the process. Absent any external perturbation, this will continue and the molecule is in a 'bright' state as photons continuously emit while excitation is present.

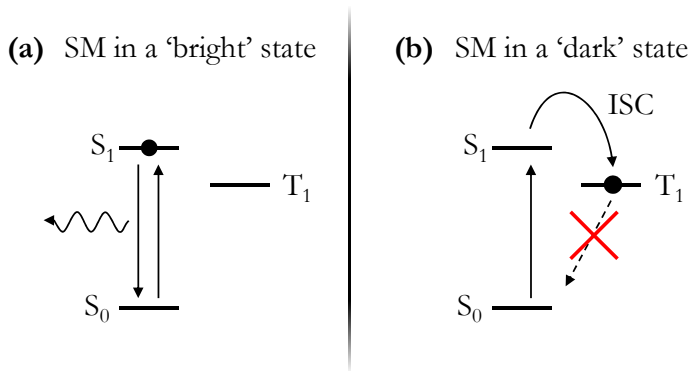

Figure 3.1. (a) Single molecule (SM) in a bright state. All absorption events lead to the emission of a photon (at first approximation) as the electron cycles through the singlet ground and excited states. (b) SM in a dark state where ISC has brough the electon to a triplet state, T_1. The transition back to the singlet ground state is forbidden and therefore relatively slow. In this time period no photon is emitted.

However, if the electron changes spin and enters a triplet state (T_1) via intersystem crossing (ISC), it can no longer relax to the ground singlet state since the $T_1 \rightarrow S_1$ transition is forbidden (slow). The molecule is now stuck in a 'dark' state and no photon is emitted until the electron can escape T_1 and return to S_0 (Figure 3.1b). The time it may remain in a dark state can be orders of magnitude longer than the time it takes for the $S_0 \leftrightarrows S_1$ cycle. This mechanism is commonly referred to as 'triplet' blinking.

It was later observed that single dyes exhibited long 'off' times that did not fit the framework of triplet blinking.[77] This was attributed to charge transfer between the excited molecule and the environment via a so-called charge transfer state (CT state). When such a state exists, excitations are quickly and non-radiatively relaxed via the environment and the molecule can stay in a dark state for as long as the CT state

exists. Prior to such observations in single molecules, non-radiative relaxation via a state similar to that of a CT state had already been developed as an explanation for blinking with long off-times in quantum dots (QD).

3.2 Charge traps in quantum dots

As blinking was first observed in QDs, the clue of a different underlying mechanism than triplet blinking was that 'off' periods lasted up to several seconds. It was initially proposed by Efros and Rosen that such blinking must come by means of a surface trap (ST) state of the QD, which acts as a reservoir for either an electron or hole.[70,78] Population of such a state has been proposed to occur via photo-ionization[79] and also through direct tunnelling[80] from the core to the surface. Irrespective of how it is populated, the effect is the same, where a so-called "spectator charge" is left in the QD core and the QD goes from a neutral state to a charged state (Figure 3.2). Even one excess charge in a small quantum dot can impose an electric field on the order of MV cm^{-1}. In other words, one charge in a typical QD volume of approximately 10 × 10 × 10 nm^3 yields a charge concentration of 10^{18} cm^{-3}. In this regime, non-radiative Auger recombination is the dominant recombination process.[81]

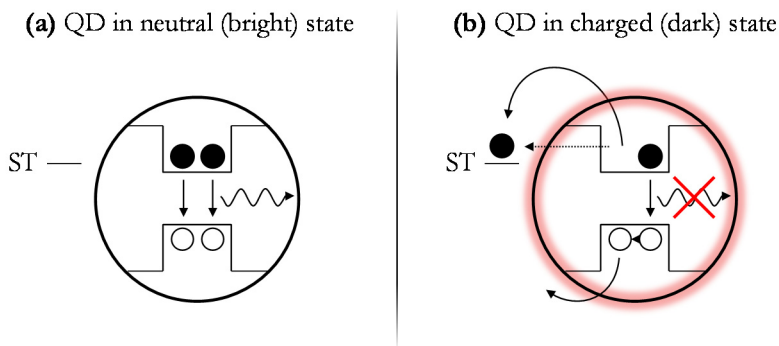

Figure 3.2. (a) QD in a neutral state where the surface trap is unoccupied. The QD is in the bright state as recombinations result in the emisson of photons. (b) QD in a charged state as an electron occupies the surface trap through either photo-ionization (solid arrow) or tunneling (dashed arrow), leaving a 'spectator' hole behind. Any excitation that forms is mediated by non-radiative Auger recombination and no photon is emitted. As the electron returns from the surface trap, the QD returns to a neutral state and photons are emitted. Electrons are drawn with black filling.

Let's assume the spectator in the charged QD state is a hole. When a subsequent photon is absorbed and generates an electron hole pair, the recombination of the charges transfer their energy to the spectator hole instead of emitting a photon. The hole is 'kicked' out to the continuum leaving the newly generated hole as the new

spectator and the QD remains charged. The rate of this process is much higher than the radiative recombination, which means all excitations release their energy via the Auger process as soon as they are formed in a charged QD. Therefore, the entire QD remains in a dark state until the electron is released from the trap state, which neutralizes the QD and emission resumes.

3.3 Energy migration in 'large' emitters

For larger multichromophoric systems, such as conjugated polymers and molecular aggregates, the picture again must change slightly. One thing the aforementioned mechanisms have in common is that the luminescence is somehow controlled by a single 'switch'. This is still true for multichromophoric systems as well, but their relatively larger size requires an additional element.

Complete blinking was demonstrated in an MEH-PPV conjugated polymer with up to 2000 repeat units.[71,82] Such blinking was attributed to a photochemically generated defect state along the polymer chain. The state was proposed to consist of a radical cation and radical anion, of which the former has been reported to act as an efficient quencher of excitations.[83] The exact chemical description of such a state is perhaps somewhat ambiguous and is more than likely different for another system, which is why it is often referred to as a photogenerated quencher.

A photogenerated quencher induces efficient de-excitation of all excited states in its vicinity. In a single molecule or a QD, the excitations are spatially confined to a small region where all 'feel' the influence of the CT state or spectator charge. This is not the case for conjugated polymers and molecular aggregates which can be one or two orders of magnitude larger. A single photogenerated quencher localized on one or a few spectroscopic units cannot directly be 'felt' by all excitations unless they are able to migrate to it. Thus, the critical element that enables blinking of large multichromophoric systems is energy migration.[84]

Blinking of large, micrometer sized semiconductor crystals has only recently been observed in hybrid perovskite semiconductor crystals.[51,52,85,86] As discussed in Chapter 2, the charge diffusion lengths in perovskites are reported to be very long.[64,87] As we can understand from blinking in large multichromophoric systems, efficient migration enables efficient quenching of excitations by a single quencher. In Paper **III** we propose a mechanism by which blinking may occur in bulk semiconductor crystals several μm in diameter.

Chapter 4
Breaking the Diffraction Limit

In this work, localization microscopy (a stochastic method) was used and further developed for the adaptation of large emitters. This chapter will present the necessary background for understanding the limitations of the method and how they can in some cases be circumvented using post-processing methods.

4.1 Light diffraction through circular aperture

Light passing through an aperture will diffract and generate an interference pattern depending on the shape of the aperture as well as its size in relation to the wavelength of the light (λ). Let's assume the aperture is a lens of diameter D and focal distance *f*. These characteristics can simply be communicated by the numerical aperture (NA = nD/2*f*). Here, the resulting interference pattern generated at a distance of ~ *f* is called an Airy disk (Figure 4.1).

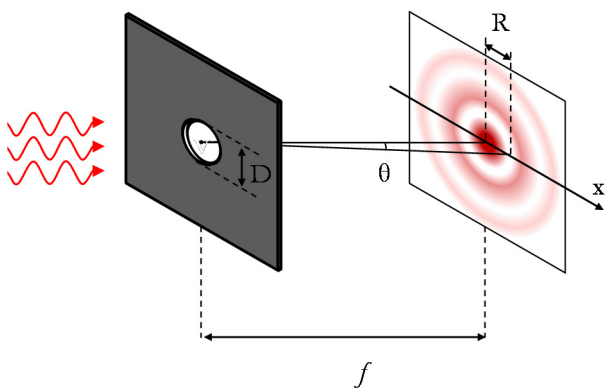

Figure 4.1. Light diffraction through circular aperture (lens) producing an Airy disk at the focal distance *f* (assuming incoming rays are parallel). R is marked as the radial distance from the center of bright dot to the first dark minimum.

The Airy disk consists of radially alternating bright and dark regions, as a result of constructive and destructive interference, which can be described by the Bessel function of the first kind ($J_1(x)$). Since spherical coordinates are better used to describe the radial dependence in the case of a circular aperture, the argument is substituted with $kasin\theta$, where $k = 2\pi/\lambda$ is the wavenumber and a is the radius of the aperture (D/2). The intensity distribution ($I(\theta)$) that makes up the Airy disk is mathematically formulated as,

$$I(\theta) = I_0 \left[\frac{2\lambda J_1(kasin\theta)}{kasin\theta} \right]^2 \tag{4.1}$$

I_0 is the intensity when $\theta = 0$, which is the central point. Since θ is the angle between the central axis and the distance to the first dark region (R), we can substitute $sin\theta$ with R/f. If we substitute a with D/2 we get the following expression for the argument of J_1,

$$kasin\theta = \frac{2\pi DR}{2\lambda f} = \frac{2\pi NAR}{\lambda} \tag{4.2}$$

where $D/2f$ has been replaced with NA.

In order to determine the radial distance from the center to the first dark region, we find the first minimum of the Bessel function J_1 and set that equal to Eq. 4.2. The first minimum of J_1 can be looked up in literature tables. Here it was also verified using MatLab where the Bessel function was plotted to find that the first minimum is equal to 3.83. Thus,

$$\frac{2\pi NAR}{\lambda} = 3.83 \tag{4.3}$$

and solving for R arrives at the all too familiar equation,

$$R = 1.22 \frac{\lambda}{2\,NA} \tag{4.4}$$

R is referred to as the resolving power of an optical system. It characterizes the smallest separation two emitting objects can have in order to be resolved with an optical instrument. The resolving power can be increased (smaller R) by either a shorter wavelength or a higher NA. In optical microscopy, the highest NA optical microscope objectives commercially available have NA ~ 1.4 which provides a

resolving power of ~ 175 nm - 300 nm in the visible range of the electromagnetic spectrum (400 nm - 700 nm), absent any aberrations of the system.

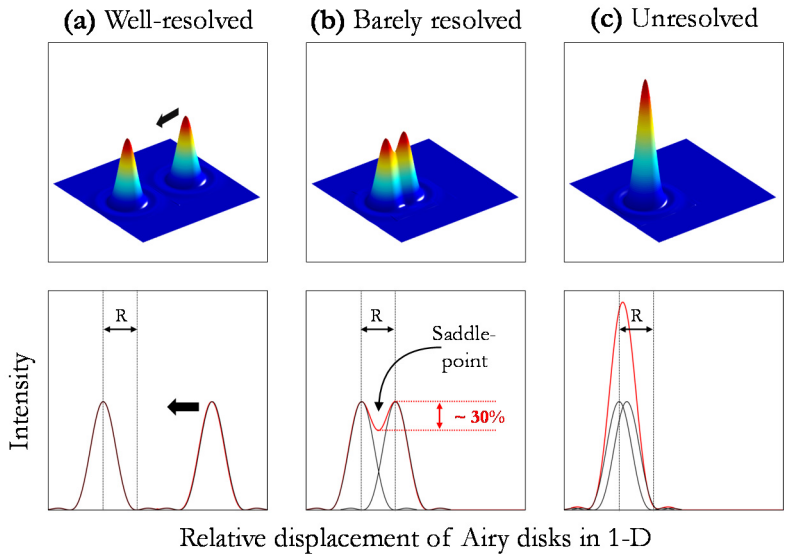

Figure 4.2. Rayleigh criterion demonstrated by the Airy disks of two point source emitters with different spatial separations. In (a) the spatial separation is >> R and the two emitters are easily resolved. (b) The spatial separation is just at the resolution limit of the optical system such that their overlapping intensities creates a 'saddle-point' that is 30% lower than the intensity of their respective peaks. This occurs at a spatial separation of R. (c) The emitters are unresovled as they are within a distance of R of one another.

The Rayleigh criterion states that if the maximum of the Airy disk generated by one object is within a distance R from the maximum of the other, they are unresolved. Figure 4.2a demonstrates two well-separated emitting objects that generate two minimally overlapping Airy disks making the objects easily resolved. When the separation is such that the peaks are separated by R (Figure 4.2b), the two emitters are just at the resolution limit of the optical system. At this point, the total intensity (red trace) at the 'saddle point' is roughly 70% of the intensity for the individual peaks (black traces). As the displacement decreases even more such that the peaks are within a distance R of each other (Figure 4.2c), one cannot distinguish the two peaks by the total intensity and the objects are unresolved.

4.1 Point spread function (PSF)

The point spread function (PSF) for an optical system is determined by imaging an object that is much smaller than the diffraction limit and characterizing the generated Airy disk through fitting (exemplified in Chapter 5). Since the PSF is unique for every system, it is important to characterize it. Preferably, an object that is as bright and as small as possible should be used so that a better precision can be acquired (see below). A diffraction limited optical system will generate an emission profile (PSF) of a small emitter where the measured distance R will be very close to the theoretical value (Eq. 4.4). Typically, the PSF will not be diffraction limited due to the unavoidable presence of aberrations, although with good optics one can get close to it. Measuring the PSF can therefore quantify the contribution of aberrations in a particular system. Another reason for characterizing the PSF is that it can actually help identify the size of an emitter when it is a few 100 nm large, as will be discussed shortly.

4.2 Approximations using Gaussian instead of Bessel

It is well-known that the diffraction pattern (Airy disk) formed by an incoherently emitting object is described with a Bessel function. Here we show that an approximation can be made with the elliptical (2D) Gaussian function.

$$G(x,y) = A * \exp\left(-\left(\frac{(x-\mu_x)^2}{2{\sigma_x}^2} + \frac{(y-\mu_y)^2}{2{\sigma_y}^2}\right)\right) + B \tag{4.5}$$

where A is the amplitude, μ_x and μ_y are the plane coordinates of the peak, σ_x and σ_y the standard deviations of the function and B the background. Eq. 4.5 is of particular relevance in localization microscopy where the location of the emitting object (μ_x, μ_y) is estimated by determining the location at I(θ= 0) of the Airy disk (Eq. 4.1). The Gaussian approximation works well as an estimator of the Bessel function[88] around the central bright spot of the Airy disk but fails to capture the real intensity distribution of the tails. However, since the amplitude of the tails is much smaller than at the peak, the relative error is not as large. Figure 4.3 shows how the two functions compare in 1D.

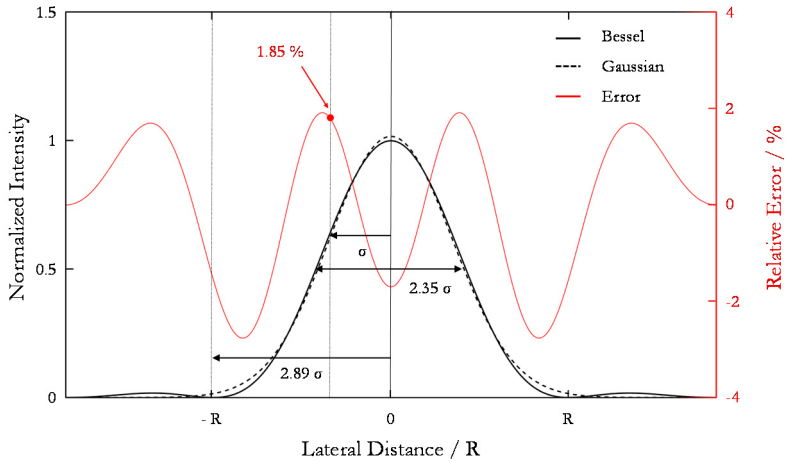

Figure 4.3. Comparison between the Bessel function (solid black trace) and Gaussian function (dashed black trace). The error relative to the peak of the Bessel function is plotted in red where it only fluctuates within a few percent. The Gaussian standard deviation parameter (width), σ, can be related to the FWHM and R with a factor of 2.35 and 2.89 respectively.

The red curve shows that the relative error of the Gaussian function compared the Bessel function is only within a few percent. Also, since the error periodically fluctuates about 0%, the integral of the two functions do not differ much at all. Thus, the Gaussian function is actually a good estimator when it comes to determining the total number of photons emitted by the object, although it may not communicate the proper spatial distribution of the photons in the image plane exactly. The volume of the elliptical Gaussian function can be calculated using,

$$V_G = 2\pi A \sigma_x \sigma_y \tag{4.6}$$

Using the Gaussian estimation, the resolution power can also be represented in terms of σ. Figure 4.3 shows that R = 2.89 σ (acquired by fitting) so it is substituted into Eq. 4.4,

$$\sigma \approx 0.42 \frac{\lambda}{2\,NA} \tag{4.7}$$

From this point forward, discussions related to the standard deviation parameter ($\sigma_{x,y}$) the term 'width' will be used. This is not to be confused with the full width at half maximum (FWHM) of the Gaussian function which is equal to $2\sqrt{2ln(2)}\sigma$ or ~2.35σ.

4.3 Localization microscopy

There are a group of methods belonging to the stochastic super-resolution methods that focus on determining the location of the Airy disk through post-processing techniques. Some of the more important and widely used ones are *stochastic optical reconstruction microscopy* (STORM)[75] and *photo-activation localization microscopy* (PALM).[89] These are typically performed in a wide-field microscope where multiple objects are imaged simultaneously. Although there is some manipulation of the excitation light involved with these particular methods, the information beyond the diffraction limit is acquired during post-processing of the data. Thus, localization microscopy can often be applied without any particular alterations to the experimental setup.

As mentioned, the center of the Airy disk communicates the real position of the emitting object to a particular degree and can be estimated with Eq. 4.5. How well this location (or 'localization' as it is referred to) can be estimated depends to a large extent on the equipment (optics, detector etc.) used to measure it, but equally so on the number of photons detected.

In the following sections, the most relevant terms pertaining to localization microscopy will be developed. It is here the originality of the thesis work can be found, which not only includes novel employment of localization microscopy for large emitters, but also the incorporation with spectroscopy in order to obtain information about the material photophysics at a nanoscopic scale.

4.3.1 Photon economy & localization precision

In any experiment, repeated measurements statistically improve the results. The same goes for localizing an emitter where each photon, n_i, provides an independent measure about the location of the emitter. When an emitter is imaged by a microscope onto a CCD camera, photons will distribute according to the microscope PSF, having a standard deviation σ_{PSF}. Regardless of how many photons arrive at the camera, they will still distribute according to the Airy disk, however, the precision will be greatly affected (Figure 4.4).

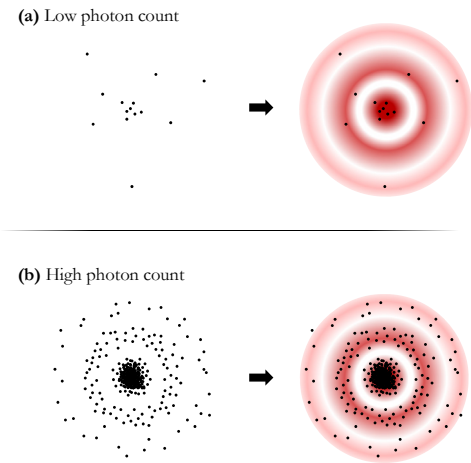

Figure 4.4. Comparison of the photon distribution in the case of a low photon count (a) and high photon count (b). Without the guided pattern of the Airy disk, the case for the low photon count does not directly communicate its pattern which leads to difficulties when applying a fit to determine its central position and width. With increasing photon count, the pattern can be seen without the guide and thereby provides for an easier task characterizing widths and position

The error in localization (localization precision, σ_N), can be acquired using,

$$\sigma_N = \frac{\sigma_{PSF}}{\sqrt{N_p}} \tag{4.8}$$

where N_p represents the total photon count. Eq. 4.8 only accounts for variation in the number of detected photons (shot-noise or Poisson noise), however, in reality there are errors related to detection as well that may affect the precision. This is particularly true when the photon flux of the emitter is low (as in the case for most single molecules). Detection errors are discussed in Chapter 5, but for now it is helpful to mention that an image generated by a CCD camera will have a background signal, (b), that is not related to any light striking the sensor but rather to the electronic function of the device. Another source of error with significance to localizing an emitter is the so-called pixelation noise. Since a CCD camera pixel has a finite size, *s*, there is an uncertainty of exactly where inside the pixel a photon strikes. Taking into account these two factors, we rewrite Eq. 4.8 as,[88]

$$\sigma_N = \sqrt{\frac{\sigma_{PSF}^2 + s^2/12}{N_p} + \frac{4\sqrt{\pi}\sigma_{PSF}^3 b^2}{sN_p^2}} \tag{4.9}$$

Here, the first term under the square root accounts for pixelation noise and the second term for background noise of the CCD camera.

4.4 Beyond the single emitter

Most optical super-resolution methods focus on the detection of individual molecules by which high-resolution imaging of small structures are obtained. This is the foundation of the stochastic functional methods and requires that the labels are attached to an object at a high enough concentration to provide a well-resolved image, but not so high such that two adjacent labels become unresolved according to the Rayleigh criterion discussed above. These methods typically find their application within the biological sciences.

In material science, however, the scenario is quite different since the objects of study are typically larger and often quite emissive. Attaching labels in such a case would be pointless since their emission would be drowned out by the emission of the sample. Although it is of interest to understand the shape and potential movement of the object, it is of greater interest to understand why an object emits. As demonstrated in Figure 4.2c, two closely spaced emitters become hard to independently localize. However, as long as the emitters are not exactly on top of one another, the widths still can provide useful information. For a collection of closely packed emitters in a particular shape (what is henceforth referred to as an *extended emitter*), a Gaussian approximation will yield widths that are larger than σ_{PSF}. The following sections will go deeper into how the standard methods presented up to this point can be adjusted to better study extended emitters.

4.4.1 Rotating elliptical Gaussian for extended emitters

The emission profiles of extended emitters should not only have larger widths but are also more likely to express asymmetry as the size of the emitter increases. This is accounted for by allowing the elliptical Gaussian function (Eq. 4.5) to rotate,

$$G(x,y,\theta) = A\exp\left(-\left(a(x_0-\mu_x)^2 + 2b(x_0-\mu_x)(y_0-\mu_y) + c(y_0-\mu_y)^2\right)\right) + B$$

$$a = \frac{cos^2\theta}{2\sigma_a^2} + \frac{sin^2\theta}{2\sigma_b^2}, \qquad b = \frac{sin\,2\theta}{4\sigma_a^2} + \frac{sin\,2\theta}{4\sigma_b^2}, \qquad c = \frac{sin^2\theta}{2\sigma_a^2} + \frac{cos^2\theta}{2\sigma_b^2} \tag{4.10}$$

Here, θ is introduced as the angle of rotation from the horizontal axis. Also, $\sigma_{x,y}$ have changed to $\sigma_{a,b}$ which are the widths along the major and minor axes of the potentially elongated and rotated emission profile. Note here that μ_x and μ_y do not need to change since they are not affected by rotation and can still be properly communicated in the x-y plane.

If one fails to allow the elliptical Gaussian to rotate, both the relative and absolute widths can be wrong. In fact, the non-rotating elliptical Gaussian only yields the right information of an elongated emission profile when it is oriented exactly along either the horizontal or vertical axes. Any orientation beyond these axes will yield an error by a factor of up to 2 (which occurs when $\theta = \pi/4$). At this orientation the non-rotating elliptical Gaussian will also incorrectly communicate that the shape is symmetrical (Figure 4.5).

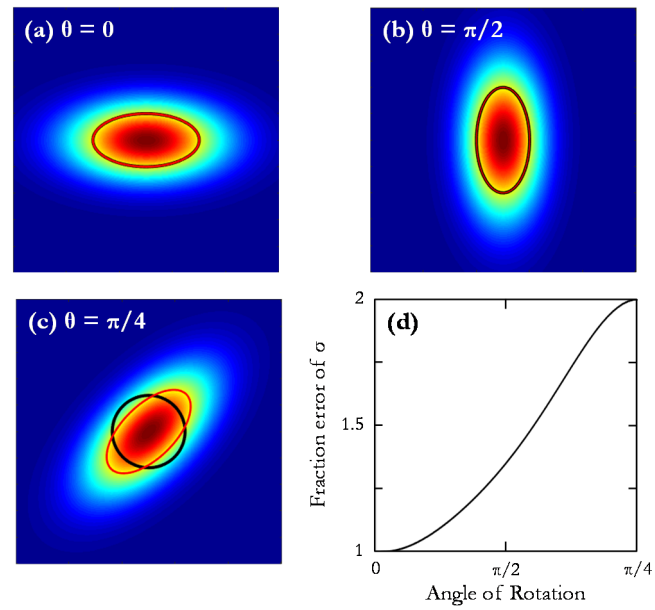

Figure 4.5. (a-b) An elongated emission profile oriented along the horizontal and vertical axes respectively. Both the non-rotating (black traces) and rotating (red traces) elliptical Gaussian functions yield the same and correct widths. (c) When the major axis of the profile is aligned at an angle of π/4 from the horizontal, the fits largely deviate where the non-rotating Gaussian incorrectly assumes a symmetric emission profile. (d) The expected error of using a non-rotating Gaussian as a function of angle of rotation.

With a more appropriate fitting function established, some of the more important parameters from Eq. 4.10 will be discussed in relation to any potential changes of the emission profile in time. A few scenarios will be given that provide a comprehensive picture of what one can expect to observe from extended emitters and how they may be interpreted.

4.4.2 Localization of extended emitters

For an extended emitter that is homogenously emitting across its entire surface, the localization will coincide with the center of mass showing only fluctuations due to detection and shot noise (Poisson noise). As the extend emitter grows, while N_P remains the same, the localization doesn't change although the localization precision decreases (larger σ_N). Luckily, the number of photons emitted by the materials in this study is a few orders of magnitude higher than that of a typical dye molecule, which means localizations can be well-trusted. Thus, if there are any fluctuations of localizations beyond what is expected based on N_p (Eq. 4.9), these must arise due to emission from the extended emitter not being temporally and spatially homogeneous. For this reason it is important to calculate the expected localization precision and compare it to the actual localization precision whenever possible. In the extreme case where part of an extended emitter goes completely dark (i.e. blinking), a large shift of the localization position may be observed. Observing such a large shift typically means some significant photophysical process has occurred, which will be exemplified in Chapter 6 (Papers **I-III**).

4.4.3 Gaussian width of extended emitters

Secondly, the widths should be understood when observed in conjunction with localization. Only observing the temporally evolving localizations from an extended emitter, with high and spatially non-fluctuating emission, cannot directly reveal whether the emitter is a single molecule or an extended emitter. Also, if the localization from one time interval to the next makes a significant shift, it cannot be determined whether an extended emitter partly "goes dark" or if there are two blinking dyes in close proximity. The width parameter together with the localization can therefore better characterize the type of emitter. The relative widths (σ_a/σ_b or vice versa) communicates the shape of the emitting region while the absolute widths can in some cases reveal the approximate size (Figure 4.6).

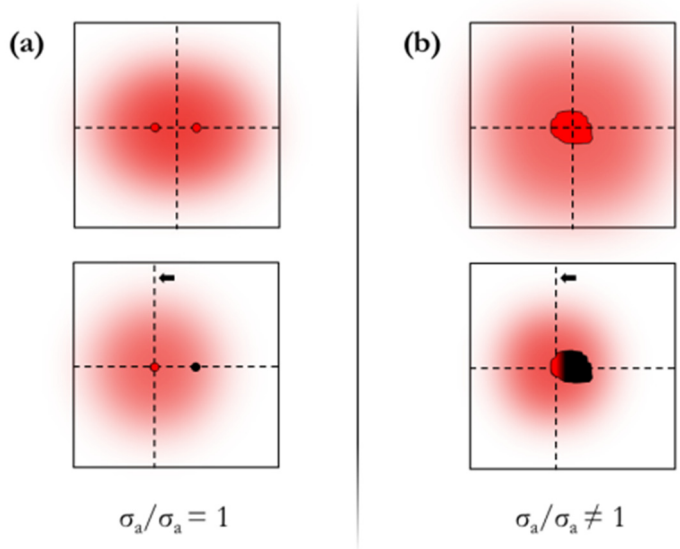

Figure 4.6. Localization shifts (dashed black lines) alone cannot distinguish between blinking of two individual emitters (a) and a partially blinking extended emitter (b). However, the width ratio in (a) communicates a symmetric profile while in (b) it is asymmetric.

4.4.4 Beyond the diffraction limit by deconvolution

The observed emission profile from an extended emitter is the time-averaged sum of multiple point sources, each generating an Airy disk in the image plane. The emission profile is the convolution between the shape of the extended emitter and the instrument PSF. Thus, even as two point emitters are in as close proximity to one another as possible, there is a very slight increase in the effective emission profile.[90]

We simulate the dependence of the width estimation on the real object size by convoluting the 2D Bessel function (representing the PSF) with artificial emitters of different sizes (Figure 4.7). The top row shows the emitter size, the middle its convolution with the PSF (the image) and the bottom row a cross-sectional comparison between the convoluted image and the PSF. Two important things to make not of: i) in the small size regime, no noticeable change is seen in the image (a-b). ii) in the large size regime, the shape of the emission profile deviates from that of a Gaussian and it becomes questionable if a good fit can be obtained (c-d).

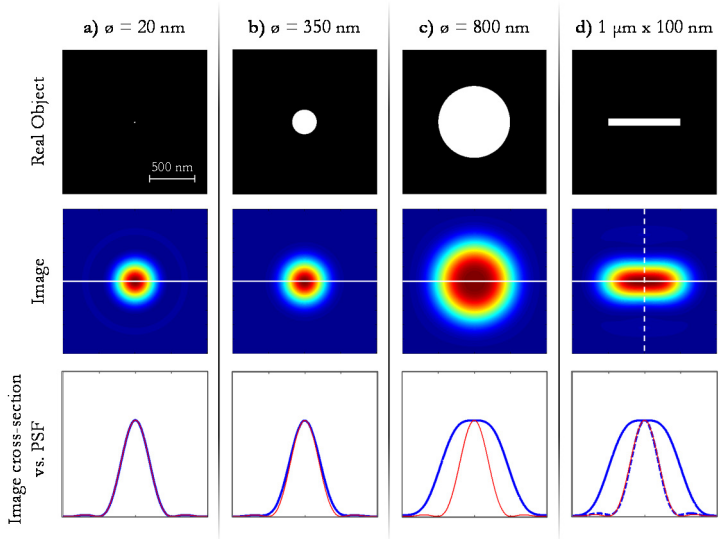

Figure 4.7. Simulation of how an artifical emitter of different size and shape (top row) convolutes with a generated PSF to create the image (middle row) as one would observe it in a microscope. The comparison between the image and PSF (bottom row) shows only a small deviation for emitter sizes up to 350 nm (a-b) and largely deviating shapes for larger objects (c-d). In this simulation, the Bessel function has the parameters representing a PSF from a diffraction limited microscope where NA = 0.6 and peak emission is at λ = 500 nm. Eqs. 4.5 and 4.8 thereby yield R ≈ 500 nm and σ ≈ 175 nm respectively.

When estimating the size of extended emitters, it is therefore important to understand how the emission profile may change in the two size regimes and how a Gaussian approximation is affected by it.

We extend the simulation for emitters ranging between 1 nm and 4 µm and assign sizes up to 350 nm to the small size regime and those above 1 µm to the large size regime. Applying the Gaussian fit to the convoluted images we understand how well it approximates the size of the emitter. Instead of the width, we compare the FWHM (FWHM = 2.35 σ) since it is a better representation of the object diameter (ø). The solid black trace in Figure 4.8b shows how well the fit approximates the diameter of the emitter (dashed black trace). The solid red trace is the fraction of the estimated size between the Gaussian and the real emitter size. It becomes clear that for sizes ø > 2µm, the fraction converges to a value of ~ 1.2. This means that even if the Gaussian is a poor approximation for the exact shape of the extended emitter in the large size regime, its diameter can still be determined using the width parameter σ. Figure 4.8b shows that the point of the Gaussian where its full width is equal to 1.2*FWHM, which coincides with the real diameter of the object. Consequently, the emitter diameter is approximately equal to 2.82 σ.

In the small size regime (Figure 4.8c) we see that the real size can still be estimated below the diffraction limit. This, however, depends on our ability to actually measure

the emission profile with a good enough precision. If the uncertainty in estimating the FWHM falls well within the range of the vertical axis scale, an estimation of the emitter size can be made even in the small size regime.

Note that this simulation assumes certain characteritics of the PSF (see caption of Figure 4.7). Using a different objective would yield different values for the plots, however, the important thing is that information beyond the diffraction limit as well as far above it can still be extracted using a simple Gaussian fit.

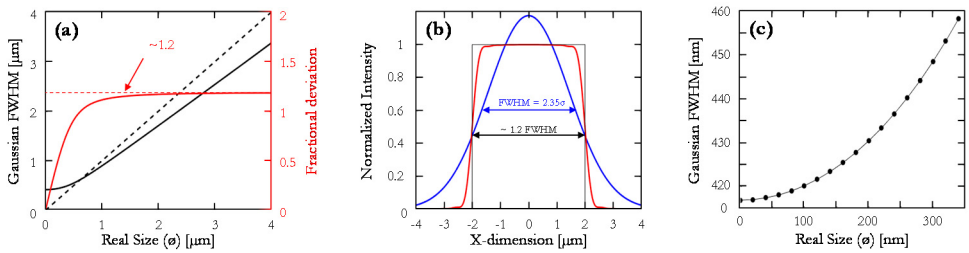

Figure 4.8. (a) Comparison between the real size of an object (dashed black trace) and the expected estimation using a Gaussian fit (solid black trace). The relative error (solid red trace) becomes constant at 1.2 for emitters larger than ~1.5 µm. (b) Large emitter regime: The real object size (black trace) convoluted with the PSF yielding the observed width in the image (red trace). A Gaussian fit (blue trace) provides a poor approximation of the size, yet its parameters can be used to estimate the real diameter of the object, which is ~ 1.2*FWHM. (c) Small emitter regime: Plot showing how the increasing width of the Gaussian estimation can still provide information about the size of the emitter.

4.4.4 Understanding the parameters: angle & rotation

The last parameter of the rotating elliptical Gaussian is the angle, θ. It was previously explained why it is important to allow the elliptical Gaussian to rotate when approximating the widths of extended emitters. This section describes how the angle actually can be used to obtain information of how many emitters are present within a large spot that is showing large temporally fluctuating intensity (blinking).

Figure 4.9 shows an example where two elongated objects (**A** and **B**) are temporally switching between emissive and nonemissive states. When both **A** and **B** are emitting, their combined intensity profile is asymmetric and therefore has an axis along which the emission profile is widest. The rotating elliptical Gaussian will therefore orient itself along this axis and yield an angle (θ_a) w.r.t. the horizontal axes. The localization will be somewhere in the middle of the two objects, which is determined by their relative intensities (dashed black lines). As either **A** or **B** become non-emissive, localization, widths, angle and intensity will change according to what is demonstrated in Figures 4.9b,c.

The development of employing the angle is rather recent which is why an extensive discussion on its proper use and interpretation would be premature at this point.

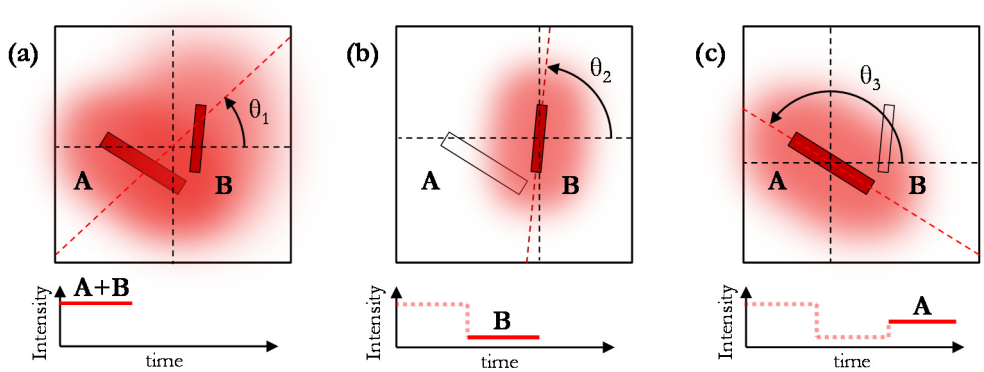

Figure 4.9. Example of two elongated emitters, **A** and **B**, switching between emissive and dark states and how the rotating Gaussian fit parameters (angle, localization and width) and intensity change accordingly.

4.5 Super-resolution Luminescence Micro-Spectroscopy

We have demonstrated how several parameters of the Gaussian function can be used to obtain quite a bit of information about the spatial features of an extended emitter. Although it is of much interest to characterize the spatial regions from where emission stems and how it may change in time, it does not directly reveal anything about why it emits. This can be done by simultaneous spectroscopic measurements which enable a study of the photophysics on a nanometer scale. We call the combination of spectroscopy and super-resolution microscopy Super-resolution Luminescence Micro-Spectroscopy (SuperLuMS), which is a method developed during this thesis work (Papers **I**, **III**, **IV**, and **VI**)

Chapter 5
Experimental Setup

As mentioned in Chapter 1, optical microscopy took a large developmental leap as detectors and light sources advanced. In practice, this meant that scientists could start manipulating the light used to probe samples in new ways, where incandescent light sources were replaced with coherent lasers possessing tunability of spectral, temporal, and intensity properties to mention a few. CCD sensors replaced the human eye and not only enabled digital imaging, but also single photon counting and spectral detection with sub-nanometer resolution (digital spectrometers). Digital imaging laid the foundation for image processing methods to develop. Complete analysis methods could now be contained in an easily distributed programming script occupying only a few kB of data storage on a computer.

The strength of the methods developed in this thesis relies on post-processing, but it is still important that the data is acquired properly so that errors are reduced. This is not only relevant to the detection related noise, but also in the measurement parameters (objective, laser source, filters etc.) that the sample is interrogated properly. Noise can be minimized in an acquisition but if the sample is probed incorrectly, the data interpretation may be wrong or greatly misguided.

In this chapter we describe the hardware of the experiment that allowed us to perform SuperLuMS. As it is not an exhaustive guide to how all measurements were performed, only the most important aspects are highlighted.

5.1 The experimental setup

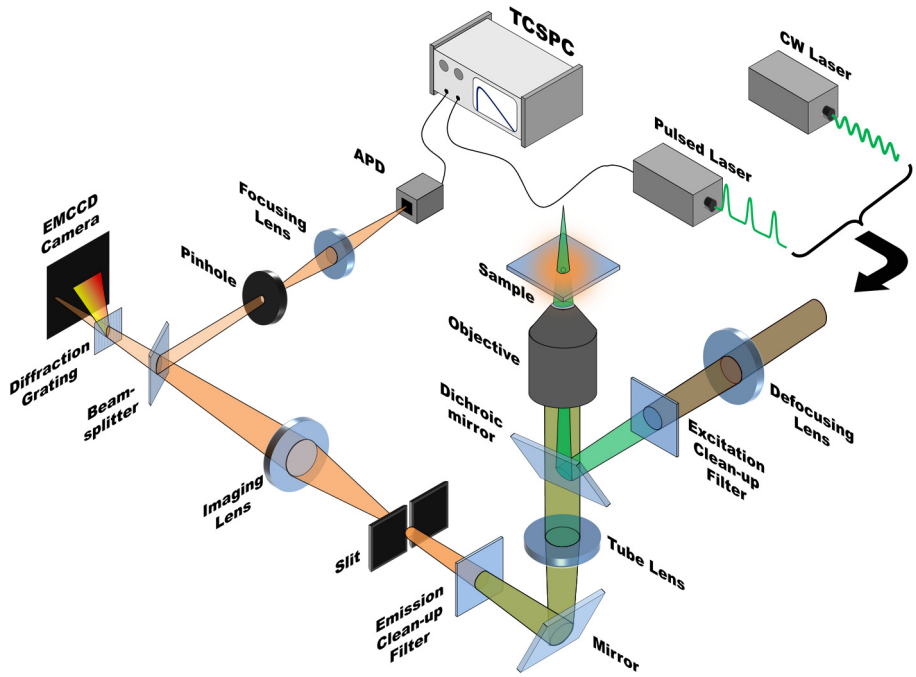

Figure 5.1. Schematic overview of the experimental setup.

A schematic overview of the experimental setup used for all measurements is shown in Figure 5.1. Depending on the experiment at hand, different excitation and detection sources were used. The system is homebuilt around an Olympus IX71 microscope base, which is inverted in its design.

5.1.1 Excitation

For continuous wave (CW) excitation we used one of the lines of an Ar^+ laser, typically either 458 nm or 514 nm. At the normal operating conditions of the laser, the power arriving at the sample was around 3 mW. When focused into a spot only a few µm diameter (confocal), this yields an excitation power density of ~10^5 W/cm^2.Using optical density filters and increasing the size of the spot (defocused imaging, see below), the typical operating regime for all experiments (with the exception of Paper **IV**) was around 0.1 W/cm^2, which is roughly equivalent to Sunlight.

For pulsed excitation, either one of three diode lasers with fixed wavelengths (405 nm, 485 nm and 640 nm) were used. All operate at repetition rates ranging from 2.5 MHz – 80 MHz. These are connected to a time-correlated single photon counting device, which also connects to an avalanche photo diode (APD) capable of detecting single photons. This configuration measures lifetime.

5.1.2 Image formation

The microscope base contains the sample holder, objective, dichroic mirror and the tube lens as shown in Figure 5.1. Additional interference filters were placed in the path of the excitation to clean it up from unwanted light generated by the lasers. Similarly for emission, extra filters were used to clean up the luminescence signal from excitation leakage through the dichroic mirror.

For this work, either a dry objective lens (40× Olympus LUCPlanFL, NA = 0.6) or an oil immersion lens was used (60× Olympus UPlanFLN, NA = 1.25). The oil immersion objective provides a higher magnification, higher light collection and better resolution but requires an immersion oil between the objective and the substrate to eliminate the refractive index mismatch. Hence, the sample must be placed such that the substrate (glass cover slip) is facing the objective rather than the sample. In such a scenario, the surface closest to the glass substrate is imaged and poses a problem if luminescence properties are to be compared with structural properties measured with an SEM (scanning electron microscope) or AFM (atomic force microscope) where the surface closest to the substrate cannot be measured. For such studies, the dry objective lens is better suited, although it comes at a cost of lower resolving power (Papers **III-IV**). One should also be mindful of which surface is being imaged if a study is made as a dependence of ambient conditions since it may differ for the two surfaces (Paper **V**).

The defocusing lens causes the light to converge which shifts the focal point away from the objective exit pupil. The result is that the field exciting the sample increases in diameter and an area of several tens of μm^2 can be imaged at the same time – defocused or wide-field imaging. Thus, by moving the defocusing lens in and out of the path we can switch between a confocal (high power) and a defocused configuration (Figure 5.2)

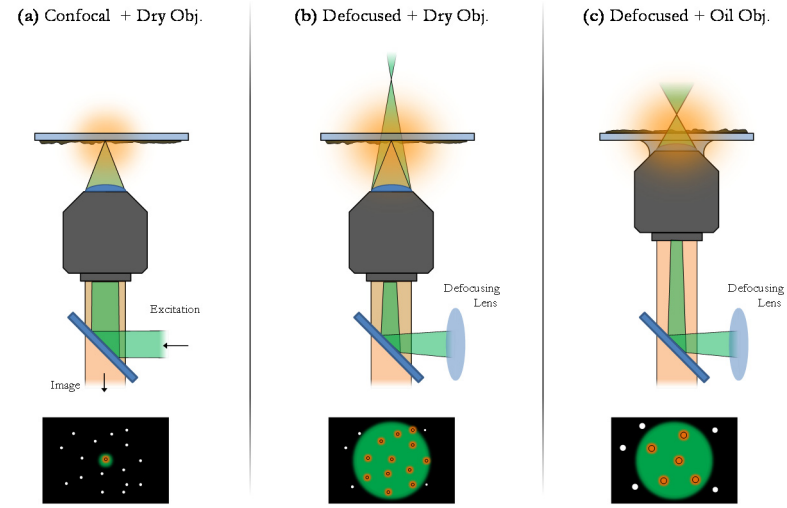

Figure 5.2. (a) Without the defocusing lens, the excitation is focused in the sample plane and only a small spot size is achieved. This is useful for excitation of a single object in a sample where the average separation is higher than ~ 5 µm. (b) Placing the defocusing lens shifts the focal point of the excitation away from the objective and the spot size increases in the focal plane of the objective leading to simultaneous excitation of multiple objects. In (a-b) the dry objective lens is used which allows the sample to directly face the objective. (c) When an oil immersion objective is used it forces the sample to face the opposite side. The bottom schematics represent individual objects that are either excited (orange) with the laser (green) or not excited (white). Using the oil immersion objective spatially reduces the field of view and objects appear larger.

At the position where the tube lens forms an image, a slit with variable width is placed to allow cropping of the image generated by the objective. This is important for spectral measurements discussed below.

5.1.2 Detection & related noise

Photons are primarily detected with an EM-CCD (electron multiplying CCD) camera (Princeton Instruments ProEM), which captures the magnified image generated by the imaging lens. The physical dimensions of each pixel is 16 µm × 16 µm, which means the effective pixel side in the EM-CCD image is s = 200 nm and s = 125 nm when using the dry objective lens and oil immersion lens respectively in conjunction with the imaging lens (added 2× magnification). The effective pixel size is important for determining the localization precision (Eq. 4.9). Spectral information is also acquired from these images (see below), which means that the EM-CCD camera is responsible for providing information in the spatial, spectral and intensity domains.

For lifetime measurements, a 50/50 beam-splitter is inserted into the path prior to the camera which thereby creates an additional image perpendicular to the path (see Figure 5.1). At this position, a pinhole (typically 100 µm in diameter) is placed which

thereby blocks the majority of the image allowing only a small region of the image to pass and focus onto the APD where lifetime is measured. Knowing the corresponding coordinates of the pinhole in the EM-CCD generated image, lifetime can be measured for specific parts of a sample by placing them at these coordinates (by moving the sample stage or imaging lens). The effective diameter of the pinhole in the image is acquired by dividing its physical diameter by the total magnification of the imaging elements (objective and imaging lens combined). The effective diameter for lifetime probing was 0.8 μm for the oil immersion objective and 1.2 μm for the dry objective.

CCD cameras are associated with three sources of noise, i) read-out noise, ii) dark noise, and iii) shot noise. The first two are strictly related to the camera and how it operates while the third is a combination of the camera features and the particle nature of light (photons). The contribution of the read-out noise can be minimized by either reducing the rate at which each image is read out from the sensor, or by increasing the exposure time. The dark noise arises from the heat-generating current that flows through the device even when no photons are detected, which will generate an unwanted signal. This can be minimized by cooling the CCD sensor. Shot noise arises due to the fact that a pixel of the CCD sensor has a finite size and the number of photons arriving at each pixel fluctuates in time. The first two sources of noise will generate a fluctuating background in the image while the third source of noise generates a fluctuation of the signal from the emitter. All three will affect the localization precision in the post-measurement analysis but can at least be accounted for as we presented in Eq 4.9.

5.1.3 Spectral measurements

To obtain spectral information from a sample, the width of the slit is minimized such that only a narrow segment of the image is passed. Placing a transmission grating before the camera causes light from the slit (vertically oriented) to diffract light before striking the imaging sensor. The same principle applies here as discussed in Section 4.1 of light diffracting through an aperture, where in this case, each groove of the grating represents a rectangular aperture. Since a grating has multiple grooves, additional interference occurs. The resulting interference pattern here will be spatially separated fringes. The orientation of the grating is such that grooves run parallel with the vertically oriented slit which causes the pattern to form horizontally on the imaging sensor. Therefore, the spatial information from the image in the slit is maintained in the vertical direction while the spatially separated intensity distribution in the horizontal direction provides spectrally resolved information at each vertical point. We call this a spectral image. The spectral resolution in the spectral image is determined by the width of the slit, the periodicity and width of the grooves in the

grating (150 grooves/mm in this case), the distance from the grating to the CCD sensor and the effective pixel size of the CCD sensor. The spectral resolution was ~2.1 nm for our microscope setup.

By employing super-resolution localization microscopy on spectral images we can simultaneously observe sub-nanometer shifts of emission w.r.t. both spectra and position. This is demonstrated in Paper **VI**.

5.1.2 PSF characterization

We mention in Section 4.1 why the characterization of the system PSF is important. To do this, we imaged fluorescent beads with an average diameter of 20 nm and a peak emission at 680 nm using the oil immersion objective with NA = 1.25. Figure 5.3a shows the emission profile of a single bead in which we applied the Gaussain fit to extract the width parameters. Figure 5.3b shows the summed intensity in both x and y dimensions (solid lines) as well as the fit (dashed lines). The width parameters from the fit were σ_x = 156 nm and σ_y = 157 nm. From Eq. 4.7, the diffraction limited widths should be 115 for λ = 680 nm. The reason the measured value deviates is partly because the measured emission from the bead is not monochromatic but mainly because there are aberrations present in our system. The Gaussian fit also reveals the background generated by the detection noise. As the Gaussian readily accounts for this (B in Eq. 4.10), the width parameters can directly be used to estimate the total number of photons detected according to Eq. 4.6.

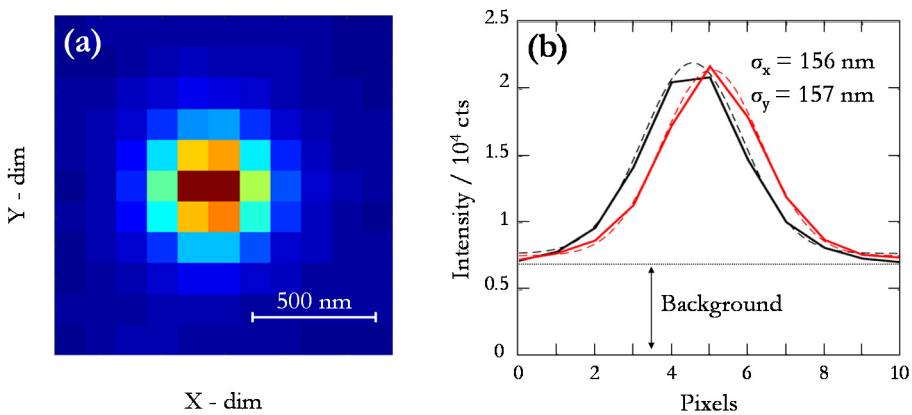

Figure 5.3. (a) RAW image of a fluorescent bead with diameter ~ 20 nm. (b) Characterization of the emission profile widths using a Gaussian fit yields σ_x = 156 nm and σ_y = 157 nm for the two dimensions (x - black, y - red). Comparing these values to the theoretical value of 115 nm reveals the presence of aberrations. The background generated by detection noise is clearly present.

Chapter 6
Results & Discussion

Herein we present the results obtained employing the super-resolution localization method together with a range of spectral measurements – the so-called SuperLuMS method. Each section gives a summary of the main findings of each Paper and puts emphasis on the contribution related to this thesis. It particularly focuses on how SuperLuMS was employed and adapted to study different luminescence phenomena leading to understanding sample specific properties. The reader is directed to the publications/manuscripts at end of this thesis for a comprehensive treatment of each result.

6.1 Paper I: Single Lévy states in J-aggregates

Perylene bisimide (PBI) J-aggregates are model systems for understanding exciton dynamics. Since they assemble into true linear aggregates, excitons are confined to move only in one dimension.[91] The majority of the theoretical framework on Frenkel excitons in fact deals with 1-dimensional systems since the theory is more easily developed.[92–94] One particular aspect that has gained some attention are so-called 'outlier' states and their effect on the photophysics. Such states have been theoretically shown to act as exciton barriers and are strongly connected to the crystal lattice disorder.[95] Paper **I** is the first experimental evidence of such outlier states. Further, Paper **I** demonstrates that an outlier state may also act as an efficient energy funnel that can influence the behavior of excitons in an entire individual J-aggregate.

The key observations leading to the interpretation that a single state is dictating the photophysics of an entire PBI J-aggregate were large amplitude blinking in strong correlation with localization and spectral shifts (Figure 6.1). Such blinking has been reported for PBI J-aggregates where it was explained that several excitons can be collectively quenched by a single photogenerated quencher. Here, it was also concluded that exciton migration lengths had to be up to 100 nm in order for such quenching to occur.[25] Paper **I** verifies those claims by the fluorescence localizations shown in Figure 6.1b. Here, two distinct clusters related to each intensity level are

seen with an average spatial separation of ~50 nm, thus suggesting that a significant part of the J-aggregate became dark (each data point in Figure 6.1b represents a mean position acquired in one frame).

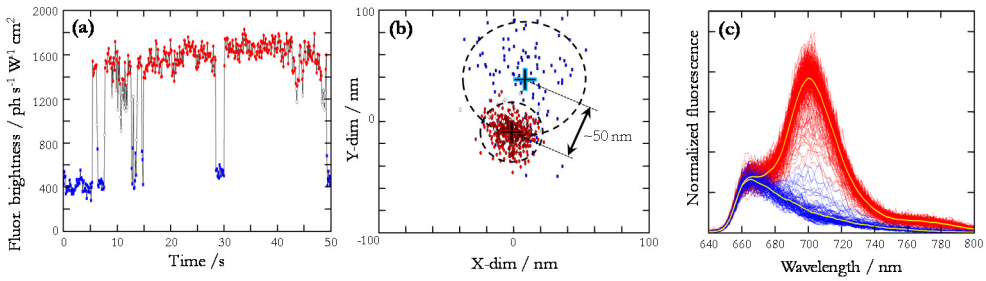

Figure 6.1. (a) Intensity trace showing blinking between two levels of a J-aggregate under CW excitation. (b) localizations from all frames of the intensity trace in (a) showing two distinct localization clusters. (c) Fluorescence spectra from each frame also showing two distinct states. Localizations and spectra from the low intensity level are plotted in blue and those from the high intensity level in red as shown in (a).

Spectral shifts were also observed with strong correlation to blinking (Figure 6.1c). At the low intensity level, the fluorescence spectrum was similar to what is expected for PBI J-aggregates in solution (blue traces). However, for the high intensity level, a drastically red-shifted peak appeared (red traces). This pointed to a single 'outlier' state that evidently controlled 75% of the excitations (considering the relative intensity between the states). Can such a state be induced by the local environment?

The main difference of the direct environment experienced by a single J-aggregate in solution and one immobilized on a substrate is that the former is dynamic while the latter is mostly static. Any interaction between a J-aggregate and the highly dynamic solution is averaged over time which means all parts of the J-aggregate are equally influenced by the environment. On a static surface, local variations of the surface properties (structural, electrostatic, etc.) may interact with different parts of the J-aggregate. Such interaction is manifested in the molecular disorder (σ_D) discussed in Chapter 2. It has been proposed that such interactions can lead to non-Gaussian distribution of disorder in the aggregate and create so-called 'outliers' - exciton states with a much lower energy than the rest of the band.[96]

To illustrate this hypothesis, two Frenkel exciton Hamiltonians (Chapter 2) for a J-aggregate containing 250 coupled monomers were generated; one using molecular disorder from a Gaussian distribution and one from a heavy-tailed Lévy distribution (Figure 6.2a). In this scheme, the Lévy distribution provides a small, yet realistic, chance for a monomer to have a very low energy.

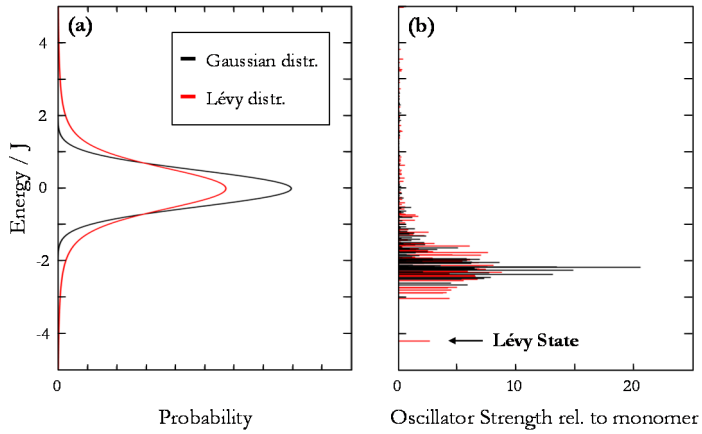

Figure 6.2. (a) Gaussian (black) and Lévy (red) probability density functions from which the molecular disorder was generated. (b) Exciton states generated by diagonalizing the Frenkel exciton Hamiltonian for 250 monomers. The x-scale is the oscillator strength relative to that of a monomer.

Diagonalizing the Frenkel exciton Hamiltonian generated with a Lévy disorder yields a clearly separated low energy state with an oscillator strength that is a few times higher than a monomer, whereas none is observed for the Hamiltonian with Gaussian disorder (Figure 6.2b). We call this a Lévy state.

As it was previously explained that a photogenerated quencher is the cause for collective blinking in J-aggregates, another contribution of Paper I is the explanation of how such a quencher can be efficient. When a J-aggregate is subject to static disorder, or so called static 'long-range interactions' of the environment, a Lévy state can also mediate efficient quenching by acting as a non-radiative energy-funnel if a photogenerated quencher forms at this site. Why a photogenerated quencher would form at a Lévy state is unknown, but one speculation is that it has to do with the fact that more excitons relax through this state than any other, which statistically increases the chance of the formation of such a quencher by a e.g. photochemical reaction.

The reason why spectral changes are observed is because of the J-aggregate size relative to exciton migration distance and the large energy gap between the Lévy state and the band. Assuming a migration of 100 nm means a J-aggregate of shorter length can be completely quenched by a single quencher. In a longer J-aggregate, some excitons would not reach the Lévy state (depending on its formation site) and would instead radiatively relax through a local minimum state with a blue-shifted energy. Consequently, when the Lévy state is inactive, emission only comes from states that are outside the migration range of excitons. Therefore, the drastic spectral changes in Figure 6.1c are a result of the 'on-off' switching of a low energy Lévy state (see Figure 6.3).

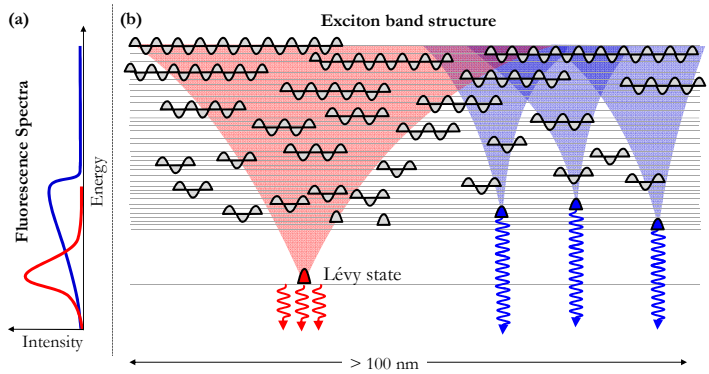

Figure 6.3. (a) Schematic of experimentally observed red-shifted peak. (b) Efficient funneling of excitons from nearly the entire individual J-aggregate (longer than 100 nm) to the Lévy state which gives rise to the red-shifted peak. Excitons far away from the Lévy state relax through local minima and contribute to the typically observed peak. Adapted from Paper **I**.

6.2 Paper II & III: PL blinking in $MAPbI_3$

As discussed in Chapter 3, blinking is an indicator of non-radiative relaxation pathways being present and it has been observed in many individual systems of different sizes. Paper **II** reports on the first observations of photoluminescence (PL) blinking of large (sub-micrometer) individual hybrid perovskite semiconductor crystals. Normalizing the typically observed blinking amplitude to the excitation power density we found it to be equivalent to ~10^5 reference dyes. Compared to the blinking amplitude observed for J-aggregates (Figure 6.1a), these $MAPbI_3$ semiconductor nano-crystals express 1000-fold larger blinking amplitudes. We thereby conclude that both non-radiative relaxation pathways and charge carrier diffusion must be extremely efficient.

Paper **II** also reports on the excitation power dependence of blinking (Figure 6.4). With increasing excitation power, the blinking amplitude decreases which goes against the understanding that non-radiative Auger recombination is responsible for blinking in inorganic quantum dots. If this were the case, blinking should be promoted with increasing excitation power density as the Auger process occurs when the excitation density is 10^{18}-10^{19} cm^{-3}. Because the studied crystals were much larger than a typical quantum dot (ø = 10 nm), the highest excitation densities achieved in our experiment were still several orders of magnitude less than what is required for the Auger process. We therefore conclude that PL blinking must be induced via a different mechanism.

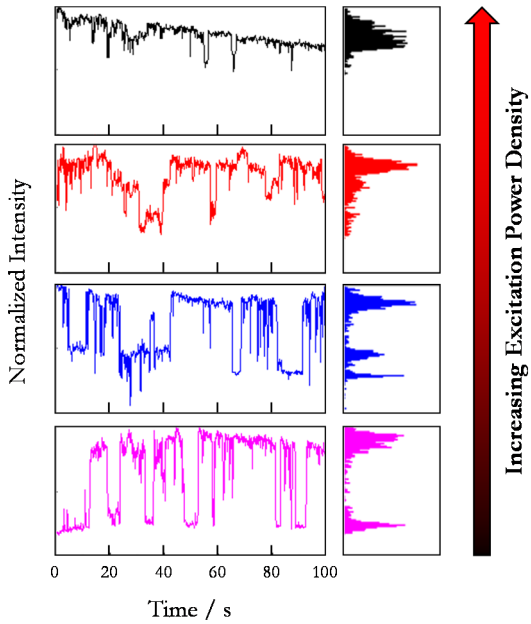

Figure 6.4. Decreasing blinking amplitude and on/off times with increasing excitation power density. The histograms reveal two or three clearly separated states for low excitation powers while at the highest excitation power both the amplitude and off-duration diminishes for the partially quenched emitter. Adapted from Paper **II**.

To understand the blinking mechanism in $MAPbI_3$ crystals, PL lifetime was measured together with blinking and localization in Paper **III** where again, a strong correlation was found. The localizations in the example presented in Figure 6.5 again show that a large part of the semiconductor crystal became nonemissive (Figure 6.5b). The switching back and forth between two intensity levels in strong correlation with localization of emission between two distinct spatial regions advocates for a single quencher that is fixed in space.

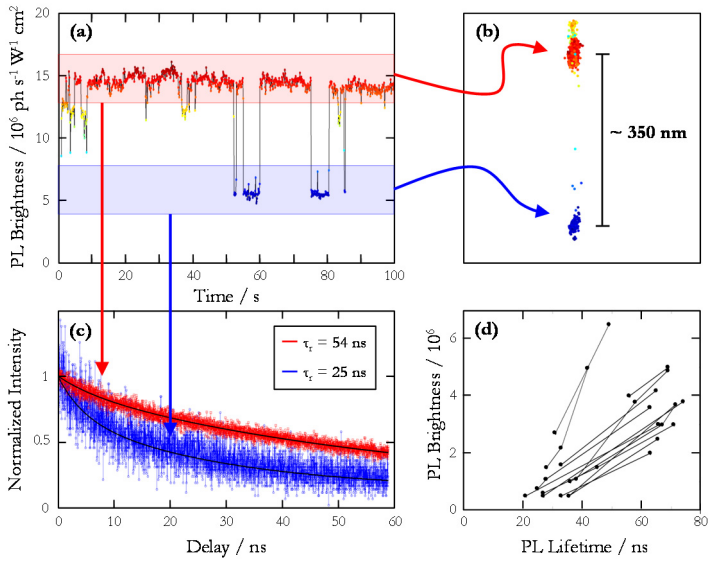

Figure 6.5. (a) PL intensity trace of a blinking crystal with two largely separated intensity levels. (b) Localizations in all frames of the acquisition with two well-separated localizations clusters belonging to each intensity level. (c) PL lifetime of the two intensity levels; τ_r = 54 ns for the high intensity level and τ_r = 25 ns for the low intensity level. (d) Lifetime statistics from 18 blinking crystals where positive correlation reveals a dynamic quenching mechanism. Data for each crystal is linked with a line. Adapted from Paper III.

PL lifetimes of the two intensity levels were significantly different (Figure 6.5c). As PL blinked down by ~60%, the PL lifetime was shortened by nearly the same relative amount (54 ns to 25 ns). This was not unique for one crystal but all studied crystals (18) showed the same positive correlation (Figure 6.5d). This means that the quenching mechanism must be dynamic.

From what is reported in the literature, material defects acting as non-radiative relaxation pathways should be present at a concentration somewhere between 10^{15}-10^{18} cm^{-3} in solution-processed $MAPbI_3$.[66,67,97,98] For the typical crystal volume used in **Paper III** (~10^8 nm^3), this corresponds to roughly 100 defects (assuming the lowest concentration). The PL quantum yield (Φ_L) was estimated to be ~2% indicating that the majority of recombination events were non-radiative and mediated via at least 100 defects/traps. With the addition of 1 similar defect, neither Φ_L nor τ_r should change as drastically as seen in Figure 6.5. Thus, blinking must be induced by a trap that is significantly more efficient in mediating non-radiative recombination than the material defects. We call this a 'super-trap'.

We propose that the super-trap is composed of one electron trap and one hole trap in close vicinity, forming a so-called donor-acceptor complex. The efficiency of such a trap is greater since highly diffusing charge carriers in both bands can be immobilized

at the same spatial coordinate and quickly recombine, leaving little to no room for charge detrapping.[97] Through activation and passivation of such a trap, large amplitude blinking is observed.

We found that the blinking related localization shifts can also reveal whether the super-trap is operating at its maximum capacity or not. If so, charge carriers in the vicinity of the super-trap would be given a greater probability to recombine radiatively, which is manifested as blinking without localization shifts. In Paper **III** we demonstrate this to occur in highly crystalline and large $MAPbI_3$ microcrystals.

The process behind the activation/passivation of the super-trap was not as easily studied and we are left to speculation. However, one thing that must be true is that the process must be slow since we can actually observe PL 'on' and 'off' times for several seconds. We therefore propose that slowly migrating species, such as ions[99,100] or even impurities, may passivate either the donor or the acceptor of the complex. This would reduce its ability to quench charge carriers to the same rate as the other defects until the passivating species leaves. Figure 6.6 summarizes our proposed model behind PL blinking in $MAPbI_3$.

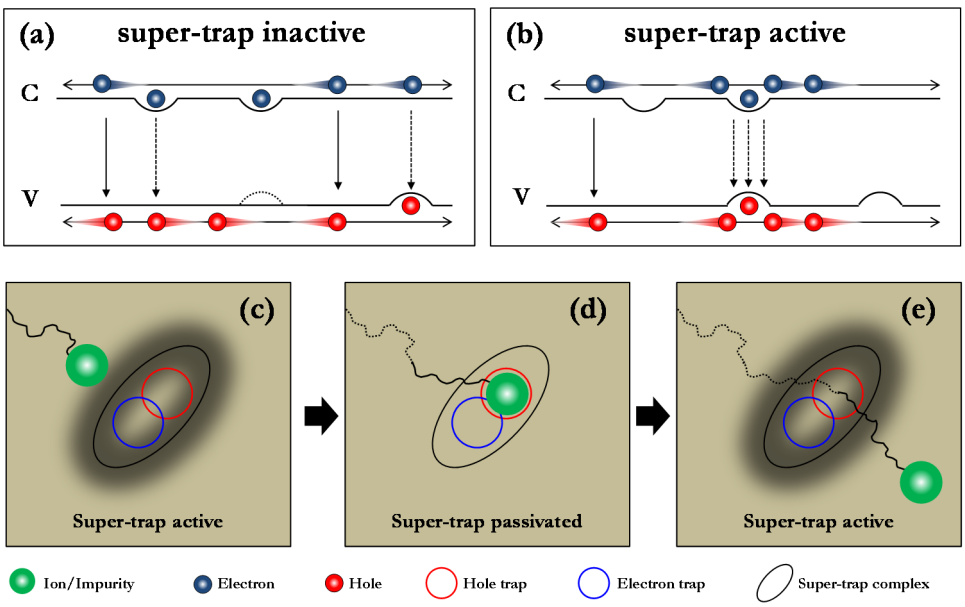

Figure 6.6. (a-b) Schematic of the bandgap with spatial coordinates on the horizontal axis. One electron trap and hole trap spatially overlap which forms the super-trap. In (a) the hole trap is passivated and non-radiative recombination is dictated by all defects in the crystal. Radiative recombination occurs directly across the bandgap. In (b) the super-trap is active and all non-radiative recombination occurs at this site. Radiative recombination only occurs in regions that are spatially separated from the super-trap by a distance surpassing the average charge diffusion length or for charges that mange to radiatively recombine before reaching the super-trap. (c-e) Mechanism of passivation by a slowly migrating species. In this example, passivation occurs of the hole trap, but could easily be the other way around. Adapted from Paper **III**.

6.3 Paper IV: Photo-induced degradation of $MAPbI_3$

Despite their rampant success on the organic photovoltaic scene, organo-metal halide perovskites suffer stability issues in different conditions.[35,59,101] Paper **IV** addresses the photo-induced degradation and aims at understanding the photophysical process behind it. Typically, observable degradation under light exposure (1 Sun) occurs on the time-scale of hours to days or even weeks,[102] which makes it hard to study the photophysical process responsible for it in real time. Thus, we increased the illumination intensity from 1 Sun to 100 Sun so that the process could develop on the time scale of seconds to minutes. This enabled us to apply SuperLuMS and observe the photo-induced degradation in real time. For solar cells, the active layer's ability to absorb light is of prime importance. By observing the gradual change of the PL quantum yield, we relate a decreasing PL intensity to either an increase in non-radiative recombination pathways or a decrease in absorption. Although the two cannot be directly distinguished by luminescence, both contribute to a degrading solar cell.

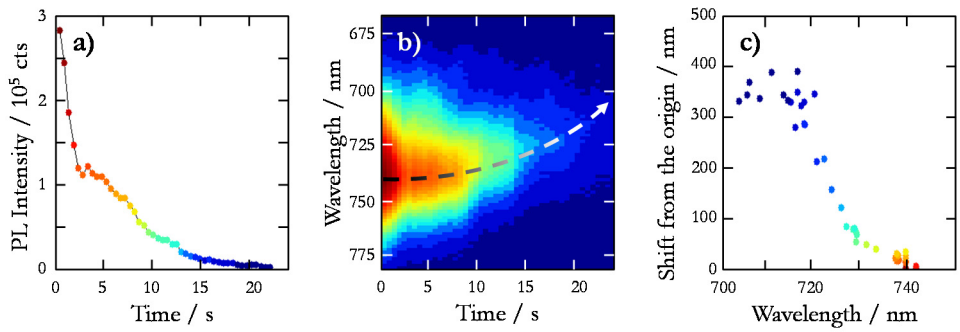

Figure 6.7. (a) PL intensity degradation correlated with (b) spectral shifts and (c) localization shifts. Adapted from Paper **IV**.

Figure 6.7a shows the PL intensity degradation of a single $MAPbI_3$ crystal occurring within 20 seconds. Of more interest for understanding the photophysics is the fact that the PL spectra gradually and significantly blue-shifts while the PL intensity decreases (Figure 6.7b). Employing the same localization method as for Papers **I-III**, we observed a large and gradual shift of the localization in correlation with degradation (Figure 6.7c).

The results in Figure 6.7 reveal that the crystal gradually becomes nonemissive from one end to the other while the part that remains emitting progressively shows a more and more blue shifted PL spectrum.

More importantly, we observed complete blinking with a particularly long 'off' period of nearly 1 minute (Figure 6.8a) during the degradation process. Both the PL intensity and the spectrum remained unchanged before and after the blinking event, from which we conclude that blinking suspends degradation. From Papers **II-III**, we understand that blinking in $MAPbI_3$ is induced by a so-called super-trap which efficiently mediates non-radiative recombination of charge carriers. Thus, there must be a link between the presence of free charge carriers and the mechanism behind photo-induced degradation in $MAPbI_3$.

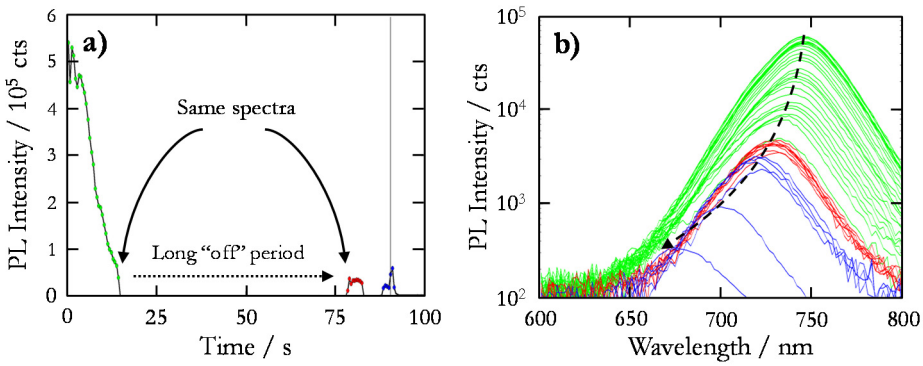

Figure 6.8. (a) Degradation of a $MAPbI_3$ crystal undergoing degradation. Blinking causes the crystal to go into a dark state for nearly 1 minute during which degradation is suspended. This can be seen in (b) where the spectra gradually blue-shifts despite the long 'off' period. Adapted from Paper **IV**.

The gradual spectral blue-shift points to an increasing bandgap, which is reportedly linked to the Pb-I-Pb bond angle.[56] Tuning the bandgap can thereby be achieved by either replacing the molecular cation (MA^+ in this case) with a cation of different size, or completely removing the MA^+ ion.[103] Increasing of the bandgap has also been reported to occur with decreasing crystallite size.[62] However, in that report a blue-shift of 15 nm occurred as the average crystallite size decreased from several μm down to a few 100 nm, which doesn't agree with our observations. Thus we rule out this as an explanation for our observations.

Migration of MA^+ has been reported to occur on slow time-scales (ms-s)[99] under the stimulus of an externally applied electric field. Although no such electric field is present in our measurement, ion migration may still be induced with the presence of mobile charges. The net charge of the optically excited crystal is zero, yet the distribution of charges may not necessarily be homogeneous. We believe charge build-up[104] at particular locations of the crystal may induce local electric fields which in turn drives ion migration. As such, increasing the optical excitation increases charge carrier density and the rate at which ions are driven from their lattice positions also increases. Complete PL blinking therefore suspends the ion migration as no charges

are present to uphold the local electric fields. What effectively occurs when more and more MA^+ are displaced is that a structural breakdown of the lattice occurs and the 3-D $MAPbI_3$ structure collapses into the 2-D PbI_2 structure. This collapse is gradual, relatively slow and should start in one particular location from where it propagates. The schematic in Figure 6.9a summarizes the proposed photo-induced process.

The photo-induced degradation was verified in a thin film sample using a color camera. Prior to degradation, red (760 nm) emission is observed while after the degradation only the typical green emission (500 nm) of PbI_2 is seen in the spot where the laser excited the sample (with the exception of a few spots). SEM images comparing a degraded and an undegraded region show faint structural differences. A transmission image shows the reduced absorption from the degraded parts (se Figures 6.9b-d).

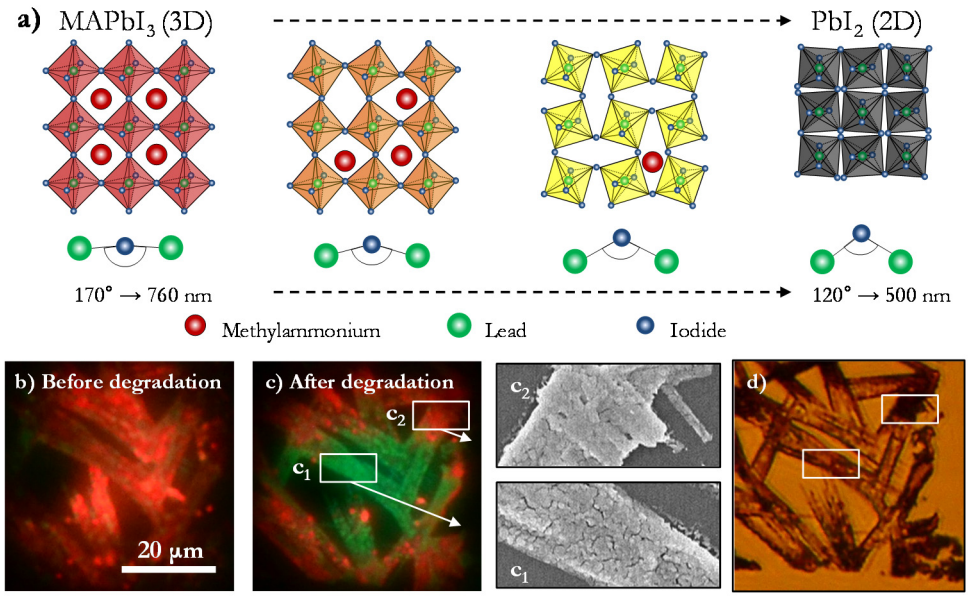

Figure 6.9. (a) Schematic showing the mechanism behind photo-induced degradation as $MAPbI_3$ (3D) collapses to PbI_2 (2D). As more MA^+ ions are driven out of their position, the structure becomes unstable and deforms. The change of the bond angle causes the bandgap to increase until finally the lattice has collapsed into PbI_2 with emission at 500 nm. (c-d) Color images taken prior to and after photo-induced degradation of the same spot. (c_1-c_2) SEM images of degraded and undegraded regions respectively where structural differences can be noticed. (d) Transmission image taken with a bright source and long pass filter with a cut-on wavelength of 514 nm reveals a redued $MAPbI_3$ absorption in the degraded regions.

6.4 Paper V: PL enhancement of $MAPbI_3$

In Paper **V** we employed a method called differential imaging, which is used in order to observe fast fluctuations of intensity on a steady or slowly changing background. Paper **V** reports on the PL enhancement[41,44,50] of micrometer sized $MAPbI_3$ polycrystals in relation to ambient conditions and spatial dimensions of the grains within the polycrystal. PL enhancement is attributed to photo-curing of trap states with the aid of ambient oxygen via the crystal surface or bulk dissolved oxygen (from synthesis in air). This process suppresses non-radiative recombination which progressively increases the PL quantum yield. PL blinking is also reported to occur in spatially defined regions that exhibit fast enhancement and high PL quantum yield. At the time Paper **V** was published we had not yet developed our current understanding of the super-trap model presented in Paper **III**, but in light of those discoveries it makes sense that blinking occurs in regions with a lower concentration of trap states since a super-trap can be more efficient.

The contribution to Paper **V** of this thesis is the differential imaging method, which allowed us to isolate the blinking regions within the polycrystal and independently study their PL dynamics. The differential imaging method highlights the PL changes from one frame to the next which therefore captures the blinking and suppresses the enhancement. With low background enhancement, the differential image reveals more or less the same information as the unprocessed PL image. However, as the bulk enhancement increases, the differential image still reveals the individual blinking regions in contrast to the normal PL image where they are obscured by the bulk PL (Figures 6.10$a_{1\text{-}2}$). From the differential image we can therefore identify spatial regions with high or low blinking activity and compare their PL transients (Figures 6.10a-b).

We also applied the localization method to all spots in each of the frames in the differential image and created a cumulative map of localizations (Figure 6.10c). According to our hypothesis of why we see an increased PL, such a map identifies regions with increased photo-curing of traps. In relation to our work in papers **II** and **III**, these are the regions where a super-trap is most efficient.

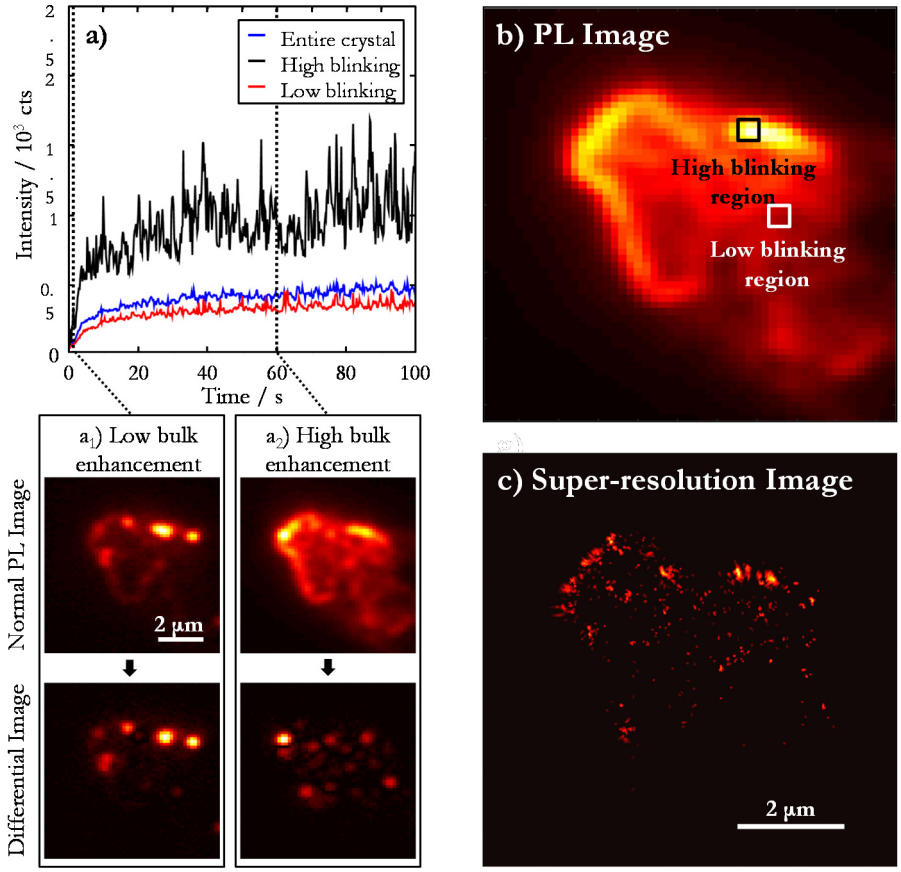

Figure 6.10. (a) PL transients of the entire polycrystal (blue), a highly blinking region (black) and a low blinking region (red). PL enhancement is seen to a different degree in all traces where the increase of the PL quantum yield is higher for the highly blinking region. (a_1-a_2) A comparison between the normal and differential image when background enhancement is low (a_1) and background enhancement is high (a_2). (c) Cumulative image of localizations revealing regions of high blinking activity and thereby pointing to low concentration of trap staes. Adapted from Paper **V**.

6.5 Paper VI: Localized phases in $MAPbI_3$ nano-rods

Paper **VI** reports on the role defects play on the tetragonal → orthorhombic phase transition (occurring somewhere in the 160 K- 140 K temperature range) of highly crystalline $MAPbI_3$ nano-rods. The two phases have different bandgaps, thus, the PL spectral change is a strong indicator from which phase emission is observed. We report on the co-existence of both phases in a single nano-rod 5 µm long and 500 nm wide. As temperature is regulated across the phase-transition, localized spots with greatly enhanced PL is observed which we relate to inclusions within the nano-rod with significantly lower defect density. We propose that regions with high defect concentration transition to the orthorhombic phase at higher temperatures compared to low-defect regions. Thus, at a given temperature, both phases may be present in a single nano-rod and independently studied.

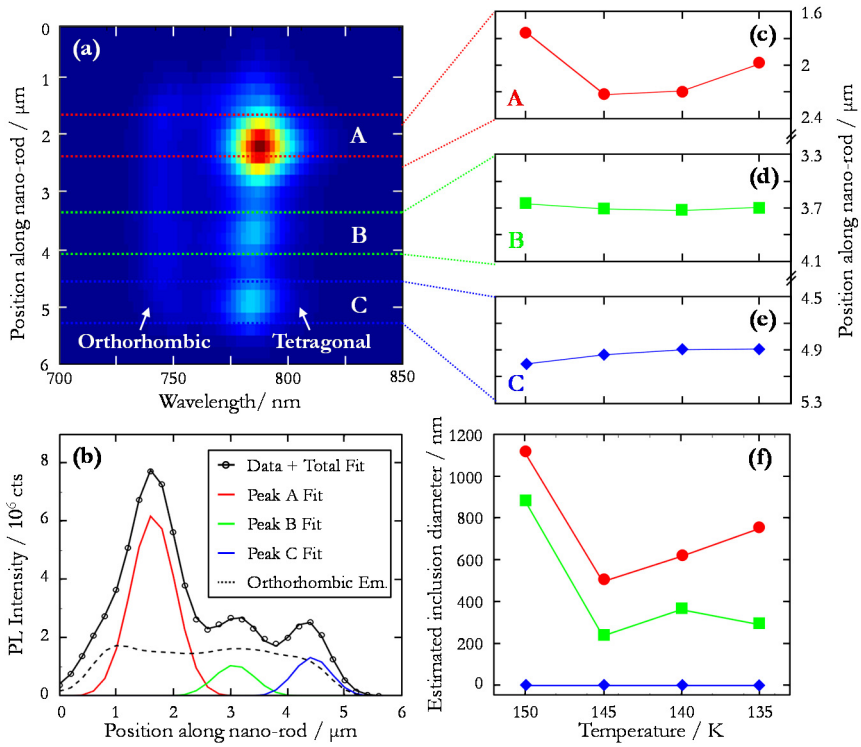

Figure 6.11. (a). Spectral image showing both the orthorhombic phase and tetragonal phase at T = 145 K. Tetragonal phase has 3 separated spots (A,B and C) of increased PL quantum yield related to reduced trap concentrations. (b) The three peaks were fitted with three 1D Gaussian functions. The shape of the orthorhombic phase (dashed black line) was used as a background in the fit. (c-e) The mean positions of each peak for all temperatures showing a large shift of peak A. (f) Estimated size of the inclusions using the deconvolution method described in Chapter 3. Shrinking of the inclusion is seen for peaks A and B but for peak C the estimated sizes are at the resolution limit of the microscope, hence, a size cannot be determined. Adapted from Paper **VI**.

We studied the two phases separately by employing the localization microscopy method on so-called spectral images (Chapter 5), which was the contribution of this thesis work to Paper **VI**. A spectral image maintains the spatial information in one dimension and spectrally resolves the signal in the other dimension. Nano-rods are therefore ideal objects to image in such a configuration since PL spectra can be extracted at every point along the rod. Furthermore, the fact that the two phases (tetragonal and orthorhombic) of $MAPbI_3$ have significantly different bandgaps, is another motivation to carefully study their spectral images.

The spectral image in Figure 6.11a spatially distinguishes the orthorhombic (high bandgap) and tetragonal phases (low bandgap). As the sample cools from 150 K – 135 K, three distinct spots appear for the tetragonal phase with significantly higher PL intensity than emission from the orthogonal phase. In Paper **IV**, we interpreted this PL enhancement as evidence for a decreased defect concentration. Localizing these spots for each temperature, we first notice that some are not diffraction limited which points to emission stemming from inclusions of the tetragonal phase of measurable size (as opposed to point emitters) within domains of the orthogonal phase (Figure 6.11f). Secondly, we observe a shrinking (decrease) and shifting of these inclusions as the temperature decreases and thereby directly 'view' the spatially resolved phase-transition (Figures 6.11c-e).

Conclusions

In this thesis we have presented a new method, SuperLuMS, and demonstrated its application to reveal the photophysics of solar cell materials. SuperLuMS was not only able to provide insight into the sizes of emitting regions but also connect a particular region to a spectroscopic feature. Luminescence blinking served as a key observation to understand the trap-related dynamics in both PBI J-aggregates and $MAPbI_3$ perovskites.

In our study on J-aggregates we presented first time experimental evidence of a so-called outlier state (Lévy state), to which energy is efficiently funneled. We have demonstrated that when such a state exists in an aggregate, it dictates the photophysics of the majority of the aggregate – a phenomenon often associated with Lévy statistics. A Lévy state may act as either a channel for radiative or non-radiative relaxation.

For perovskites, we have reported on complete blinking of nano- and micro-crystals that are orders of magnitude larger than a quantum dot. Blinking of such large objects is remarkable and we attribute it to efficient quenching by a single trapping state (super-trap). We have proposed that such a trap acts as an electron donor-acceptor complex which is able to immobilize highly diffusing charges in one and the same location so that they can quickly recombine non-radiatively.

With SuperLuMS we were also able to monitor slow photochemical processes in $MAPbI_3$ nano-crystals and larger bulk crystals. First, we demonstrate that with increasing excitation power, degradation occurs on the time scale of seconds. Blinking led us to understand that the mechanism leading to degradation is dictated by photo-induced migration of methylammonium ions (MA^+) away from their lattice position. SuperLuMS revealed that the degradation process occurs gradually as a structural collapse that initiates in a particular location and extends progressively outward.

At lower excitation powers, we show that photoluminescence enhancement occurs as a response to photo-curing of material defects. Using a method called differential imaging together with localization microscopy, we were able to identify local regions of rapidly increasing photoluminescence, suggesting these regions have a lower concentration of defects. The reason for such inhomogeneous distribution of photoluminescence enhancement is something that requires further study.

Finally we have demonstrated the applicability of super-resolution localization imaging on so-called spectral images of a $MAPbI_3$ nano-rod. As temperature was decreased from 160 K to 130 K (across the tetragonal-orthorhombic phase transition), we observed greatly enhanced PL emission from the tetragonal phase in very localized regions. We were able to characterize the width and position of these spots and observe their shifts in space during the transition.

Acknowledgments

To rightfully express my gratitude to all the people that have supported me or somehow been a part of this endeavor, I should surely write another thesis. I am truly humbled by the experience I have had the last 5 years at the Chemical Physics department and cannot thank all those involved enough.

First and foremost, I want to express my gratitude to my supervisor, Ivan. Through more ways than one, you have not only taught me a great deal about Science, but also that there is always a solution to a problem (which generally can be found in the workshop). I would be fortunate if I could retain even a fraction of what you know. Your knowledge in the field impresses me, but more so your drive and passion for it. It has indeed been a pleasure being your student and I thank you sincerely for taking me on. Tõnu, I also want say thank you for assuming the responsibility to co-supervise me. I extend a special thank you to you, Villy, for being an inspiration to us all. Arkady, Donatas (my friend), Ebbe, Per, Jens, Eva & Torbjörn, you help this place flourish both academically and socially. Thank you for providing a positive environment.

I am grateful for the collaboration with prof. Frank Würthner and his group. Thank you for providing us with excellent samples.

A special thanks goes to you Yuxi. I can't express how much I value having worked with you. Eva, thank you for always being quick to reply to my questions and also for helping me review parts of the thesis. Thank you, Jens, for your advice in thesis writing.

To the members of the Chemical Physics department, and in particular the SMS group, thank you for providing a fun working place. Because of you I enjoy coming to the department every day. Rafa, thank you for introducing me.

I also want to extend a thank you to those who I have had the opportunity to collaborate with at Lund University. Sune and Mikkel, you were the first who supported me 8 years ago and have done so ever since. I can with confidence say I wouldn't be where I am today without your guidance and friendship. Edouard, thank you for investing your time and energy into the AFSIN network. I hope we can continue working together in support of Africa.

I want to dedicate a special paragraph to my friends and co-workers within the AFSIN network. I can speak on the behalf of all of us when I say that we are all extremely grateful for the support from ISP. Thank you Ernst, thank you Carla and all those working with you. Jeremie, your undying devotion to AFSIN does not go unnoticed. I am happy that I met you and look forward to what we can do in the future.

To the lads, Michele, Victor, Lloyd, Christian, your support in these years has been boundless. A PhD is no breeze and you have been there throughout with wise advice…and a few brews.

To all my friends around the area, thank you for providing me ample opportunity to disconnect from work and do things 'normal' people do.

Dabalataan, kaadhimaa koo Feenet, jaalalli kee dhugaa, deeggarsi yaada keetii, kolfi kee inni gammachuun na guutu jajjabina addaa naaf ta'ee dadhabbii malee fiixan ba'e. Jaalalli keenyaa dhugaa Gadaan nufaana haa waaru.

My deepest gratitude is to my family. I have been fortunate to have you close to me during these years and many before. I cannot find words that explain how much you mean to me. This is as much your accomplishment as it is mine, I couldn't have done it without you. I love you deeply.

I am a man of faith and sincerely believe that nothing goes without the grace of God. He has truly blessed me with all these wonderful people in my life and continues to add to it. I am eternally grateful to Him.

References

1. Moerner, W. E. & Kador, L. Optical-detection and spectroscopy of single molecules in a solid. *Phys. Rev. Lett.* **62,** 2535–2538 (1989).
2. Orrit, M. & Bernard, J. Single pentacene molecules detected by fluorescence excitation in a p-terphenyl crystal. *Phys. Rev. Lett.* **65,** 2716–2719 (1990).
3. Basché, T. & Moerner, W. E. Optical modification of a single molecule in a solid. *Nature* **355,** 335–337 (1992).
4. Tian, Y., Navarro, P. & Orrit, M. Single molecule as a local acoustic detector for mechanical oscillators. *Phys. Rev. Lett.* **113,** 135505 (2014).
5. Ambrose, W. P. & Moerner, W. E. Fluorescence spectroscopy and spectral diffusion of single impurity molecules in a crystal. *Nature* **349,** 225–227 (1991).
6. Sako, Y. *et al.* Single molecule imaging of signaling molecules in living cells. *Single Mol.* **1,** 159–163 (2000).
7. Giepmans, B. N. G., Adams, S. R., Ellisman, M. H. & Tsien, R. Y. The fluorescent toolbox for assessing protein location and function. *Science* **312,** 217–224 (2006).
8. Betzig, E. & Trautman, J. K. Near-field optics - microscopy, spectroscopy, and surface modification beyond the diffraction limit. *Science* **257,** 189–195 (1992).
9. Hell, S. W. & Wichmann, J. Breaking the diffraction resolution limit by stimulated emission: stimulated-emission-depletion fluorescence microscopy. *Opt. Lett.* **19,** 780–782 (1994).
10. Hell, S. W. Far-field optical nanoscopy. *Science* **316,** 1153–1158 (2007).
11. www.nobelprize.org/nobel_prizes/chemistry/laureates/2014/.
12. Patterson, G., Davidson, M., Manley, S. & Lippincott-Schwartz, J. Superresolution imaging using single-molecule localization. *Amnu Rev Phys Chem* **61,** 345–367 (2013).
13. Lippincott-Schwartz, J. & Manley, S. Putting super-resolution fluorescence microscopy to work. *Nat. Methods* **6,** 21–23 (2009).
14. Leung, B. O. & Chou, K. C. Review of super-resolution fluorescence microscopy for biology. *Appl. Spectrosc.* **65,** 967–980 (2011).
15. Park, H., Hoang, D. T., Paeng, K. & Kaufman, L. J. Localizing exciton recombination sites in conformationally distinct single conjugated polymers by super-resolution fluorescence imaging. *ACS Nano* **9,** 3151–3158 (2015).

16. Habuchi, S., Onda, S. & Vacha, M. Mapping the emitting sites within a single conjugated polymer molecule. *Chem. Commun.* 4868–4870 (2009).

17. Jelley, E. E. Spectral absorption and fluorescence of dyes in the molecular state. *Nature* **138,** 1009–1010 (1936).

18. Schiebe, G. Über die veränderlichkeit der absorptionsspektren in lösungen und die nebenvalenzen als ihre ursache. *Angew. Chemie* **50,** 212–219 (1937).

19. Würthner, F., Kaiser, T. E. & Saha-Möller, C. R. J-aggregates: from serendipitous discovery to supramolecular engineering of functional dye materials. *Angew. Chemie Int. Ed.* **50,** 3376–3410 (2011).

20. Fidder, H., Knoester, J. & Wiersma, D. A. Optical properties of disordered molecular aggregates - a numerical study. *J. Chem. Phys.* **95,** 7880 (1991).

21. Fidder, H., Terpstra, J. & Wiersma, D. A. Dynamics of frenkel excitons in disordered molecular aggregates. *J. Chem. Phys.* **94,** 6895–6907 (1991).

22. Kaiser, T. E., Wang, H., Stepanenko, V. & Würthner, F. Supramolecular construction of fluorescent J-aggregates based on hydrogen-bonded perylene dyes. *Angew. Chem. Int. Ed. Engl.* **46,** 5541–5544 (2007).

23. Yao, H. *et al.* Superstructures of mesoscopic monomolecular sheets of thiacyanine J-aggregates in solution. *Langmuir* **19,** 8882–8887 (2003).

24. Eisele, D. M., Knoester, J., Kirstein, S., Rabe, J. P. & Vanden Bout, D. A. Uniform exciton fluorescence from individual molecular nanotubes immobilized on solid substrates. *Nat. Nanotechnol.* **4,** 658–663 (2009).

25. Lin, H. *et al.* Collective fluorescence blinking in linear J-aggregates assisted by long-distance exciton migration. *Nano Lett.* **10,** 620–626 (2009).

26. Tian, Y., Stepanenko, V., Kaiser, T., Würthner, F. & Scheblykin, I. G. Reorganization of perylene bisimide J-aggregates: from delocalized collective to localized individual excitations. *Nanoscale* **4,** 218–223 (2012).

27. Mohammad Bagher, A. Comparison of organic solar cells and inorganic solar cells. *Int. J. Renew. Sustain. Energy* **3,** 53–58 (2014).

28. Kojima, A., Teshima, K., Shirai, Y. & Miyasaka, T. Organometal halide perovskites as visible-light sensitizers for photovoltaic cells. *J. Am. Chem. Soc.* **131,** 6050–6051 (2009).

29. Snaith, H. J. Perovskites: The emergence of a new era for low-cost, high-efficiency solar cells. *J. Phys. Chem. Lett.* **4,** 3623–3630 (2013).

30. Brenner, T. M., Egger, D. A., Kronik, L., Hodes, G. & Cahen, D. Hybrid organic—inorganic perovskites: low-cost semiconductors with intriguing charge-transport properties. *Nat. Rev. Mater.* **1,** 15007 (2016).

31. Dittrich, T. *et al.* Diffusion length of photo-generated charge carriers in layers and powders of $CH_3NH_3PbI_3$ perovskite. *Appl. Phys. Lett.* **109,** 73901 (2016).

32. Shen, Q. *et al.* Optical absorption, charge separation and recombination dynamics in sn/pb Cocktail perovskite solar cells and their relationships to the photovoltaic performance. *J. Mater. Chem. A* **3,** 9308–9316 (2015).

33. Ball, J. M. *et al.* Optical properties and limiting photocurrent of thin-film perovskite solar cells. *Energy Environ. Sci.* **8,** 602–609 (2015).

34. Stranks, S. D. *et al.* Electron-hole diffusion lengths exceeding 1 micrometer in an organometal trihalide perovskite absorber. *Science* **342,** 341–344 (2013).

35. Berhe, T. A. *et al.* Organometal halide perovskite solar cells: degradation and stability. *Energy Environ. Sci.* **9,** 323–356 (2016).

36. Deng, Y. *et al.* Scalable fabrication of efficient organolead trihalide perovskite solar cells with doctor-bladed. *Energy Environ. Sci.* **8,** 1544–1550 (2015).

37. Babayigit, A., Ethirajan, A., Muller, M. & Conings, B. Toxicity of organometal halide perovskite solar cells. *Nat. Mater.* **15,** 247–251 (2016).

38. Dongqin Bi *et al.* Efficient luminescent solar cells based on tailored mixed-cation perovskites. *Sci. Adv.* **2,** e1501170 (2016).

39. Song, Z. *et al.* Impact of processing temperature and composition on the formation of methylammonium lead iodide perovskites. *Chem. Mater.* **27,** 4612–4619 (2015).

40. Aldibaja, F. K. *et al.* Effect of different lead precursors on perovskite solar cell performance and stability. *J. Mater. Chem. A* **3,** 9194–9200 (2015).

41. Tian, Y. *et al.* Mechanistic insights into perovskite photoluminescence enhancement: light curing with oxygen can boost yield thousandfold. *Phys. Chem. Chem. Phys.* **17,** 24978–24987 (2015).

42. Tian, Y. *et al.* Enhanced organo-metal halide perovskite photoluminescence from nanosized defect-free crystallites and emitting sites. *J. Phys. Chem. Lett.* **6,** 4171–4177 (2015).

43. Fang, H. H., Wang, F., Adjokatse, S., Zhao, N. & Loi, M. A. Photoluminescence enhancement in formamidinium lead iodide thin films. *Adv. Funct. Mater.* **26,** 4653–4659 (2016).

44. Noel, N. K. *et al.* Enhanced photoluminescence and solar cell performance via lewis base passivation of organic-inorganic lead halide perovskites. *ACS Nano* **8,** 9815–9821 (2014).

45. DeQuiletttes, D. W. *et al.* Photo-induced halide redistribution in organic–inorganic perovskite films. *Nat. Commun.* **7,** 11683 (2016).

46. Zheng, K. *et al.* Trap states and their dynamics in organometal halide perovskite nanoparticles and bulk crystals. *J. Phys. Chem. C* **120,** 3077–3084 (2016).

47. Wu, X. *et al.* Trap states in lead iodide perovskites. *J. Am. Chem. Soc.* **137,** 2089–2096 (2015).

48. DeQuilettes, D. W. *et al.* Impact of microsctructure on local carrier lifetime in perovskite solar cells. *Science* **348,** 683–686 (2015).

49. Bischak, C. G., Sanehira, E. M., Precht, J. T., Luther, J. M. & Ginsberg, N. S. Heterogeneous charge carrier dynamics in organic–inorganic hybrid materials: nanoscale lateral and depth-dependent variation of recombination rates in methylammonium lead halide perovskite thin films. *Nano Lett.* **15,** 4799–4807 (2015).

50. Shao, S. *et al.* The effect of the microstructure on trap-assisted recombination and light soaking phenomenon in hybrid perovskite solar cells. *Adv. Funct. Mater.* **26,** 8094–8102 (2016).

51. Tian, Y. *et al.* Giant photoluminescence blinking of perovskite nanocrystals reveals single-trap control of luminescence. *Nano Lett.* **15,** 1603–1608 (2015).

52. Yuan, H. *et al.* Photoluminescence blinking of single-crystal methylammonium lead iodide perovskite Nanorods induced by surface traps. *ACS Omega* **1,** 148–159 (2016).

53. Grancini, G. *et al.* $CH_3NH_3PbI_3$ perovskite single crystals: surface photophysics and their interaction with the environment. *Chem. Sci.* **6,** 7305–7310 (2015).

54. Pelant, I. & Valenta, J. *Luminescence spectroscopy of semiconductors.* (Oxford University Press, 2012).

55. Saba, M. *et al.* Correlated electron–hole plasma in organometal perovskites. *Nat. Commun.* **5,** 5049 (2014).

56. Filip, M. R., Eperon, G. E., Snaith, H. J. & Giustino, F. Steric engineering of metal-halide perovskites with tunable optical band gaps. *Nat. Commun.* **5,** 5757 (2014).

57. Fang, H.-H. *et al.* Photophysics of organic-inorganic hybrid lead iodide perovskite single crystals. *Adv. Funct. Mater.* **25,** 2378–2385 (2015).

58. Osherov, A. *et al.* The impact of phase retention on the structural and optoelectronic properties of metal halide perovskites. *Adv. Mater.* (2016). doi:10.1002/adma.201604019

59. Yuan, H. *et al.* Degradation of methylammonium lead iodide perovskite structures through light and electron beam driven ion migration. *J. Phys. Chem. Lett.* **7,** 561–566 (2016).

60. Merdasa, A. *et al.* Super-resolution luminescence micro-spectroscopy reveals mechanism of photo-Induced degradation in CH3NH3PbI3 perovskite nano-crystals. *J. Phys. Chem. C* **120,** 10711–10719 (2016).

61. Hutter, E. M. *et al.* Direct–indirect character of the bandgap in methylammonium lead iodide perovskite. *Nat. Mater.* **1**. (2016). doi:10.1038/nmat4765

62. D'Innocenzo, V., Srimath Kandada, A. R., De Bastiani, M., Gandini, M. & Petrozza, A. Tuning the light emission properties by band gap engineering in hybrid lead halide perovskite. *J. Am. Chem. Soc.* **136,** 17730–17733 (2014).

63. Hutter, E. M., Eperon, G. E., Stranks, S. D. & Savenije, T. J. Charge carriers in planar and meso-structured organic–inorganic perovskites: mobilities, lifetimes, and concentrations of trap states. *J. Phys. Chem. Lett.* **6,** 3082–3090 (2015).

64. Dong, Q. *et al.* Electron-hole diffusion lengths > 175 um in solution-grown $CH_3NH_3PbI_3$ single crystals. *Science* **347,** 967–970 (2015).

65. Manser, J. S. & Kamat, P. V. Band filling with free charge carriers in organometal halide perovskites. *Nat. Photonics* **8,** 737–743 (2014).

66. Draguta, S. *et al.* Spatially non-uniform trap state densities in solution-processed hybrid perovskite thin films. *J. Phys. Chem. Lett.* **7,** 715–721 (2016).

67. Xing, G. *et al.* Low-temperature solution-processed wavelength-tunable perovskites for lasing. *Nat. Mater.* **13,** 476–480 (2014).

68. Basche, T., Kummer, S. & Brauchle, C. Direct spectroscopic observation of quantum jumps of a single-molecule. *Nature* **373,** 132–134 (1995).

69. Nirmal, M. *et al.* Fluorescence intermittency in single cadmium selenide nanocrystals. *Nature* **383,** 802–804 (1996).

70. Efros, A. F. & Rosen, M. Random telegraph signal in the photoluminescence intensity of a single quantum dot. *Phys. Rev. Lett.* **78,** 1110–1113 (1997).

71. Vanden Bout, D. *et al.* Discrete intensity jumps and intramolecular electronic energy transfer in the spectroscopy of single conjugated polymer molecules. *Science* **277,** 1074–1077 (1997).

72. Hofkens, J. *et al.* Probing photophysical processes in individual multichromophoric dendrimers by single-molecule spectroscopy. *J. Am. Chem. Soc.* **122,** 9278–9288 (2000).

73. Uno, S. *et al.* A spontaneously blinking fluorophore based on intramolecular spirocyclization for live-cell super-resolution imaging. *Nat. Chem.* **6,** 681–689 (2014).

74. Burnette, D. T., Sengupta, P., Dai, Y., Lippincott-Schwartz, J. & Kachar, B. Bleaching/blinking assisted localization microscopy for superresolution imaging using standard fluorescent molecules. *Proc. Natl. Acad. Sci.* **108,** 21081–21086 (2011).

75. Rust, M. J., Bates, M. & Zhuang, X. W. Sub-diffraction-limit imaging by stochastic optical reconstruction microscopy (STORM). *Nat Methods* **3,** 793–795 (2006).

76. Dertinger, T., Colyer, R., Iyer, G., Weiss, S. & Enderlein, J. Fast, background-free, 3D super-resolution optical fluctuation imaging (SOFI). *Proc. Natl. Acad. Sci.* **106,** 22287–22292 (2009).

77. Yeow, E. K. L., Melnikov, S. M., Bell, T. D. M., De Schryver, F. C. & Hofkens, J. Characterizing the fluorescence intermittency and photobleaching kinetics of dye molecules immobilized on a glass surface. *J. Phys. Chem. A* **110,** 1726–1734 (2006).

78. Efros, A. L. & Nesbitt, D. J. Origin and control of blinking in quantum dots. *Nat. Nanotechnol.* **11,** 661–671 (2016).

79. Kuno, M., Fromm, D. P., Hamann, H. F., Gallagher, a. & Nesbitt, D. J. Nonexponential 'blinking' kinetics of single CdSe quantum dots: A universal power law behavior. *J. Chem. Phys.* **112,** 3117 (2000).

80. Kuno, M., Fromm, D. P., Hamann, H. F., Gallagher, A. & Nesbitt, D. J. 'On'/'off' fluorescence intermittency of single semiconductor quantum dots. *J. Chem. Phys.* **115,** 1028–1040 (2001).

81. Van Driel, H. M. Kinetics of high-density plasmas generated in Si by 1.06- and 0.53-m picosecond laser pulses. *Phys. Rev. B* **35,** 8166–8176 (1987).

82. Hu, D. H., Yu, J. & Barbara, P. F. Single-molecule spectroscopy of the conjugated polymer MEH-PPV. *J. Am. Chem. Soc.* **121,** 6936–6937 (1999).

83. Wagner, R. W., Lindsey, J. S., Seth, J., Palaniappan, V. & Bocian, D. F. Molecular optoelectronic gates. *J. Am. Chem. Soc.* **118,** 3996–3997 (1996).

84. Lin, H. Z. *et al.* Fluorescence blinking, exciton dynamics, and energy transfer domains in single conjugated polymer chains. *J. Am. Chem. Soc.* **130,** 7042–7051 (2008).

85. Zhu, F. *et al.* Shape evolution and single particle luminescence of organometal halide perovskite nanocrystals. *ACS Nano* **9,** 2948–2959 (2015).

86. Wen, X. *et al.* Mobile charge-induced fluorescence intermittency in methylammonium lead bromide perovskite. *Nano Lett.* **15,** 4644–4649 (2015).

87. Li, Y. *et al.* Direct observation of long electron-hole diffusion distance in $CH_3NH_3PbI_3$ perovskite thin film. *Sci. Rep.* **5,** 14485 (2015).

88. Thompson, R. E., Larson, D. R. & Webb, W. W. Precise nanometer localization analysis for individual fluorescent probes. *Biophys. J.* **82,** 2775–2783 (2002).

89. Betzig, E. *et al.* Imaging intracellular fluorescent proteins at nanometer resolution. *Science* **313,** 1642–5 (2006).

90. Francia, G. T. Di. Resolving power and information. *J. Opt. Soc. Am.* **45,** 497–501 (1955).

91. Marciniak, H., Li, X.-Q., Würthner, F. & Lochbrunner, S. One-dimensional exciton diffusion in perylene bisimide aggregates. *J. Phys. Chem. A* **115,** 648–654 (2011).

92. Van der Auweraer, M. & Scheblykin, I. One-dimensional J-aggregates: Dependence of the properties of the exciton band on the model of the intermolecular coupling. *Chem. Phys.* **275,** 285–306 (2002).

93. Malyshev, V. & Moreno, P. Hidden structure of the low-energy spectrum of a one-dimensional localized Frenkel exciton. *Phys. Rev. B* **51,** 14587–145936 (1995).

94. Malyshev, V. A., Kozlov, G. G., Glaeske, H. & Feller, K. H. Channels of the exciton-exciton annihilation in one-dimensional aggregates at low temperature. *Chem. Phys.* **254,** 31–38 (2000).

95. Eisfeld, A., Vlaming, S. M., Malyshev, V. A. & Knoester, J. Excitons in molecular aggregates with Lévy-type disorder: anomalous localization and exchange broadening of optical spectra. *Phys. Rev. Lett.* **105,** 137402 (2010).

96. Vlaming, S., Malyshev, V. & Knoester, J. Localization properties of one-dimensional Frenkel excitons: Gaussian versus Lorentzian diagonal disorder. *Phys. Rev. B* **79**, 205121 (2009).

97. Stranks, S. D. *et al.* Recombination kinetics in organic-inorganic perovskites: Excitons, free charge, and subgap states. *Phys. Rev. Appl.* **2**, 34007 (2014).

98. Shi, D. *et al.* Low trap-state density and long carrier diffusion in organolead trihalide perovskite single crystals. *Science* **347**, 519–522 (2015).

99. Eames, C. *et al.* Ionic transport in hybrid lead iodide perovskite solar cells. *Nat. Commun.* **6**, 7497 (2015).

100. Yuan, Y. & Huang, J. Ion migration in organometal trihalide perovskite and its impact to photovoltaic efficiency and stability. *Acc. Chem. Res.* **49**, 286–293 (2016).

101. Conings, B. *et al.* Intrinsic thermal instability of methylammonium lead trihalide perovskite. *Adv. Energy Mater.* **5**, 1500477 (2015).

102. Misra, R. K. *et al.* Temperature- and component-dependent degradation of perovskite photovoltaic materials under concentrated sunlight. *J. Phys. Chem. Lett.* **6**, 326–330 (2015).

103. Xiao, C. *et al.* Mechanisms of electron-beam-induced damage in perovskite thin films revealed by cathodoluminescence spectroscopy. *J. Phys. Chem. C* **119**, 26904–26911 (2015).

104. Craciun, N. I. *et al.* Hysteresis-free electron currents in poly(p-phenylene vinylene) derivatives. *J. Appl. Phys.* **107**, 124504 (2010).

Printed by Media-Tryck, Lund University 2017 | Nordic Ecolabel 3041 0903

Congratulations, you have figured out how to see beyond the 'Blur' limit. Hopefully this urges you to continue to strive to see perhaps more things that are hidden throughout this thesis which does not meet the eye at first sight.

Our curiosity brings us to look closer at the unseen. As nature places certain limits on how small objects we can directly observe, it has merely posed a challenge for humankind to still attain information that may be obscured. Just as there are clever ways to obtain the information from the blurred text above, there are methods to acquire information of the smallest building blocks and processes in nature.

"Obsaan aannan Goromsaa dhuga.

!Obsan warrooman!"

- Oromo Proverb

LUND UNIVERSITY

Division of Chemical Physics
Department of Chemistry
Faculty of Science
ISBN 978-91-7422-496-2